

POLITECNICO DI TORINO

Master's Degree in
AUTOMOTIVE ENGINEERING



Master's Degree Thesis

Calibration of an Automotive Three-Way Catalyst Model Based on Synthetic Gas Bench Experiments

Supervisors

Prof. Federico MILLO

Prof. Luciano ROLANDO

Dr. Fabrizio GULLINO

Candidate

Giuseppe CASTELLANO

OCTOBER 2021

Abstract

Nowadays, the Three-Way Catalyst (TWC) is the standard solution employed in the automotive industry to cut down CO , HC , and NOx tailpipe emissions of vehicles equipped with gasoline engines.

The current trend towards more stringent regulations and severe testing procedures is pushing the design of modern propulsion and after-treatment systems to higher levels of complexity. This is especially true in the case of high-performance applications, for which compliance with the requirements of type approval is a serious task to accomplish. Therefore, it is necessary to develop numerical models embedding properly defined kinetic schemes, that can predict, robustly and accurately, the catalyst performances under various operating conditions. In fact, this is of paramount importance for effective optimization of the entire powertrain, with relevant savings in terms of both time and costs compared to experimental campaigns.

Within this framework, this Master Thesis aims to build and calibrate a model of a TWC currently adopted by Ferrari, utilizing a one-dimensional (1D) multi-physics fluid-dynamic code, GT-SUITE.

The required data set for the calibration of the global kinetic scheme, already defined by Ferrari according to the catalyst formulation, comes from a dedicated extensive experimental characterization performed at the Synthetic Gas Bench (SGB) by the REACT laboratory of the Queen's University of Belfast (QUB) on a catalyst sample extracted from the full-size monolith.

The experiments include isothermal OSC tests as well as light-off tests conducted under a temperature ramp from 100°C to 500°C and involving representative simple mixtures made of few selected species. This characterization methodology is mandatory to be able to separately analyze and calibrate the fundamental reactions occurring inside the catalyst, such as CO and HC oxidation and NO reduction, together with oxygen storage on Cerium sites. In addition, also complex mixtures of synthetic gases are fed to the reactor to further investigate peculiar interactions, for instance the effect of H_2O on CO oxidation and the $NO-C_3H_8$ reaction.

The tuning of the several kinetics parameters that define the chemical mechanisms, along with the active site densities and the inhibition functions, is performed exploiting the Genetic Algorithm optimization tool embedded in the software. This tool turns out to be very effective in minimizing an objective function generally defined as the cumulative absolute error between the simulated and measured outlet concentration of the considered species.

The calibrated model is finally validated over a light-off test involving a representative full mixture of the real exhaust gas at the inlet.

The results show a substantial improvement in the catalyst performance predictivity with respect to the baseline kinetic scheme. The T50s, i.e. the temperatures at which each pollutant species reaches 50% of conversion efficiency, are much well correlated with the experimental evidence.

However, limitations directly related to the lack of secondary oxidation and reduction pathways in the definition of the kinetics scheme become evident from the calibration activity. Future steps will then focus on the implementation of the necessary reactions, including also the pathways for N_2O and NH_3 formation, as well as the modifications required to improve the OSC behavior.

Table of Contents

List of Tables	IV
List of Figures	V
Acronyms	VII
1 Introduction	1
1.1 Exhaust Gas Emissions of ICE	2
1.1.1 Gaseous Pollutants Formation Mechanisms	3
1.2 The Three-Way Catalyst	5
1.3 1D Modelling and Calibration of TWC	10
2 Experimental Characterization on Synthetic Gas Bench (SGB)	17
2.1 Experimental Set-Up	18
2.1.1 Warm-Up Tests	20
2.1.2 OSC Tests	21
2.1.3 Light-Off Tests	23
3 Model Development and Calibration	29
3.1 Kinetics Scheme Definition	30
3.2 Thermal Correlation	33
3.3 Kinetics Scheme Calibration	37
3.3.1 Baseline Model Results	38
3.3.2 Step #1: OSC Calibration	38
3.3.3 Oxidation Reactions Calibration	44
3.3.4 Reduction Reactions Calibration	52
3.4 Model Validation	56
4 Conclusions	61
Bibliography	63

List of Tables

1.1	Test protocol to characterize TWC operation by means of SGB experiments	12
2.1	TWC specifications	17
2.2	Rich-to-lean average time to get $\lambda = 1.01$	23
2.3	Average engine-out emissions over NEDC, WLTC and FTP75 driving cycles	23
2.4	SGB light-off full mixture composition for performance testing . . .	24
2.5	Performance testing - CO , C_3H_6 , THC , NO light-off temperatures	27
2.6	Gas mixture compositions for light-off detailed testing. Balanced N_2	27
3.1	TWC global reactions scheme [12]	32
3.2	Reaction rates expressions	33
3.3	DoE approach for thermal correlation	34
3.4	Kinetics scheme calibration sequence	38
3.5	Rate constant of reaction #15 (k_{15}) at the three OSC temperature setpoints	41
3.6	OSC calibration - GA setup	41
3.7	Step #1: OSC optimization results	42
3.8	Step #2: optimization results	44
3.9	Step #3: optimization results	46
3.10	Step #4: optimization results	46
3.11	Step #5: optimization results	49
3.12	Step #6: optimization results	52
3.13	Step #7: optimization results	52
3.14	Step #8: optimization results	54

List of Figures

1.1	4-Stroke SI engine cycle	2
1.2	Average composition of exhaust gases from a gasoline vehicle [1] . .	4
1.3	The effect of temperature on TWC conversion efficiency (Bresch-Pietri, Leroy, and Petit, 2013)	6
1.4	Three-Way Catalytic Converter Efficiency [3]	7
1.5	Schematic structure of a TWC [4]	8
1.6	Individual steps of a simple, heterogeneous catalytic fluid–solid reaction $A_1 \rightarrow A_2$ carried out on a porous catalyst (Dittmeyer & Emig, 2008)	9
1.7	1D ATS model development and calibration process [6]	10
1.8	Schematic view of laboratory Synthetic Gas Bench [6]	11
1.9	Example of GA output for a two-parameters optimization	14
2.1	Left and Right bank monoliths with core locations	18
2.2	Reactor unit with pre-heating quartz tube removed from furnace and mixing plate exposed	19
2.3	Inlet and outlet core temperatures traces for tests #1 & #4	20
2.4	Inlet and outlet λ measurements from the three isothermal OSC tests	22
2.5	Light-off Tests protocols	25
2.6	Light-off Full Mixture Performance Test	26
2.7	Light-off Simplified Mixture Detailed Test #1: $CO + O_2$	28
3.1	1D reactor-scale TWC model calibration process	29
3.2	1D CFD model of reactor-scale TWC built in GT-SUITE v2020 . .	30
3.3	DoE approach test results on T ramp #5	35
3.4	Thermal correlation results on the five warm-up tests	36
3.5	Thermal correlation results on T Ramp #5	37
3.6	Full mixture performance testing. Baseline schemes (R&S and Ferrari). Experimental and simulated outlet species concentrations .	39
3.7	Full mixture performance testing. Baseline schemes (R&S and Ferrari). Experimental and simulated conversion efficiencies	40

3.8	Example of Arrhenius plot [13]	41
3.9	Arrhenius plot used for linear regression	42
3.10	OSC test #1: 300°C. CO , O_2 , CO_2 and λ traces	43
3.11	OSC test #2: 400°C. CO , O_2 , CO_2 and λ traces	43
3.12	OSC test #3: 500°C. CO , O_2 , CO_2 and λ traces	44
3.13	$CO + O_2$ light-off test. (a) CO , O_2 , CO_2 and $T CAT OUT$ traces. (b) CO conversion efficiency.	45
3.14	$C_3H_6 + O_2$ light-off test. (a) C_3H_6 , O_2 , CO_2 and $T CAT OUT$ traces. (b) C_3H_6 conversion efficiency.	47
3.15	$C_3H_8 + O_2$ light-off test. (a) C_3H_8 , O_2 , CO_2 and $T CAT OUT$ traces. (b) C_3H_8 conversion efficiency.	48
3.16	$CO + O_2 + H_2O$ light-off test. (a) CO , H_2O , CO_2 and $T CAT OUT$ traces. (b) CO conversion efficiency.	50
3.17	$CO + C_3H_6 + C_3H_8 + H_2O + O_2$ light-off test. (a) CO , C_3H_6 , C_3H_8 and $T CAT OUT$ traces. (b) CO , C_3H_6 , C_3H_8 and THC conversion efficiencies.	51
3.18	$CO + NO$ light-off test. (a) CO , NO , CO_2 and $T CAT OUT$ traces. (b) CO and NO conversion efficiencies.	53
3.19	$CO + NO$ light-off test. Experimental outlet species concentrations	54
3.20	$C_3H_6 + NO$ light-off test. (a) C_3H_6 , NO , CO_2 and $T CAT OUT$ traces. (b) C_3H_6 and NO conversion efficiencies.	55
3.21	$C_3H_6 + NO$ light-off test. Experimental outlet species concentrations	56
3.22	Full mixture performance testing. Optimized model. Experimental and simulated temperature profiles	57
3.23	Full mixture performance testing. Optimized model. Experimental and simulated outlet species concentrations	58
3.24	Full mixture performance testing. Optimized model. Experimental and simulated conversion efficiencies	59

Acronyms

ICE

Internal Combustion Engine

EGR

Exhaust Gas Recirculation

ATS

After-Treatment System

SI

Spark Ignition

CI

Compression Ignition

HC

Unburnt Hydrocarbons

TWC

Three-Way Catalyst

PGM

Platinum Group Metals

OSC

Oxygen Storage Capacity

SGB

Synthetic Gas Bench

GA

Genetic Algorithm

cGPF

Coated Gasoline Particulate Filter

FTIR

Fourier Transform Infra-Red Spectroscopy

cpsi

Cells per Square Inch

GHSV

Gas Hourly Space Velocity

WGS

Water-Gas Shift

AA

Advanced Adaptive

dx

Discretization Length

dt

Simulation Master Time Step

DoE

Design of Experiments

Chapter 1

Introduction

In the last decades, exhaust emissions associated with Internal Combustion Engines (ICE) powered vehicles have become a serious matter of concern with regard to the global warming and the environmental pollution problem. Starting from the early 90's, public institutions in Europe began to introduce regulations as countermeasures to push the automotive industry towards the production of cleaner and more environmental-friendly engines. The evolution of the legislation regarding the type approval of new vehicles and the consequent enforcement of increasingly stringent limits led to the development of different technologies for emissions abatement. Nowadays, complex after-treatment systems (ATS) made-up of different devices installed in the exhaust line, accompanied by advanced in-cylinder emissions control strategies, i.e. Exhaust Gas Recirculation (EGR), and innovative hybrid architectures, represent an almost standard mix of solutions in the actual car market. The design of an ATS and its on-board integration is therefore a fundamental aspect to be taken into account during the development of any new propulsion system. This is especially true in the case of high-performance applications, for which compliance with the legislative requirements is a serious task to accomplish. In particular, it is of paramount importance to develop numerical models that can predict, robustly and accurately, the ATS operation under various working conditions. In fact, this is the key for an effective optimization of the entire powertrain, with relevant savings in terms of both time and costs compared to experimental campaigns.

Within this framework, this Master Thesis aims to build and calibrate a model of a Three-Way Catalyst (TWC) currently adopted by Ferrari, utilizing a one-dimensional (1D) multi-physics fluid-dynamic code, GT-SUITE.

The required data set for the calibration comes from a dedicated extensive experimental characterization performed at the Synthetic Gas Bench (SGB) by the REACT laboratory of the Queen's University of Belfast (QUB).

1.1 Exhaust Gas Emissions of ICE

Internal Combustion Engines are mechanical devices able to convert the chemical energy stored into a fuel in mechanical energy. The conversion occurs through the combustion process, during which the fuel releases its chemical energy when reacting with a proper amount of air inducted inside the cylinder. The heat produced increases the pressure of the gas mixture, that is exploited by the so-called crank mechanism to produce mechanical work at the crankshaft, so torque. Since the combustion process changes the characteristics of the fuel, engine operation can be maintained only through a periodic replacement of the in-cylinder charge. In fact, the working cycle of a conventional 4-strokes ICE is made up of 4 phases:

1. Intake
2. Compression
3. Expansion/Power
4. Exhaust

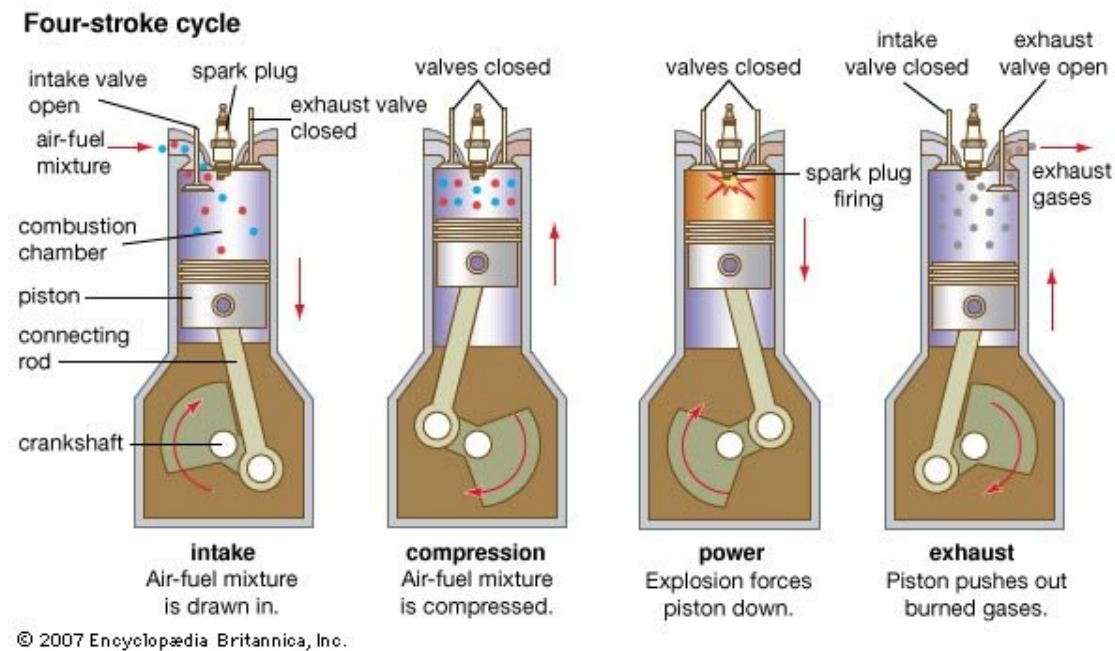
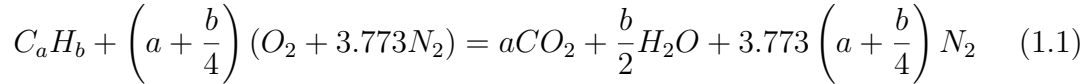


Figure 1.1: 4-Stroke SI engine cycle

The combustion process is initiated towards the end of the compression stroke by a spark in the case of Spark Ignition (SI) engines (figure 1.1), or by the direct

injection of the fuel itself inside the combustion chamber in the case of modern Compression Ignition (CI) engines.

The complete and ideal burning of a generic hydrocarbon blend, such as petrol fuels for transportation, with oxidizer air can be basically described by the following reaction:



Accordingly, the products of a complete ideal combustion would be in principle non-toxic: carbon dioxide (CO_2), water vapour (H_2O), and nitrogen (N_2).

However, it is necessary to underline that the real process is much more complex, and the oxidation of a fuel molecule takes place indeed through a large amount of intermediate steps. Unfortunately, several unavoidable phenomena occur leading to a deviation from the ideal process and consequently to the formation of unwanted toxic pollutants, generally about 1-2% of all combustion products (figure 1.2). The most important of them, the ones that after-treatment devices are designed to deal with, are listed here below:

- Carbon Monoxide, **CO**
- Unburnt Hydrocarbons, **HC**
- Nitrogen Oxides, **NO_x**
- Particulate Matter, **PM**

Although CO_2 is not harmful to human beings, and therefore it is not considered as a pollutant, it is a greenhouse gas. Being a product of ideal combustion, there is no other way to minimize it than to reduce the fuel consumption, i.e. improving the engine efficiency.

1.1.1 Gaseous Pollutants Formation Mechanisms

CO formation mechanisms

Carbon monoxide, CO , is the major pollutant for SI engines.

As said before, the fuel oxidation process is made of a huge amount of intermediate reactions that eventually lead to the oxidation of CO into CO_2 . However, this last step is far slower with respect to all the previous ones. At this point, there are two concurrent causes for CO formation:

1. Engine operation under rich mixture. The air-fuel ratio (A/F) is lower than the corresponding stoichiometric value (around 14.6 for gasoline), i.e. the

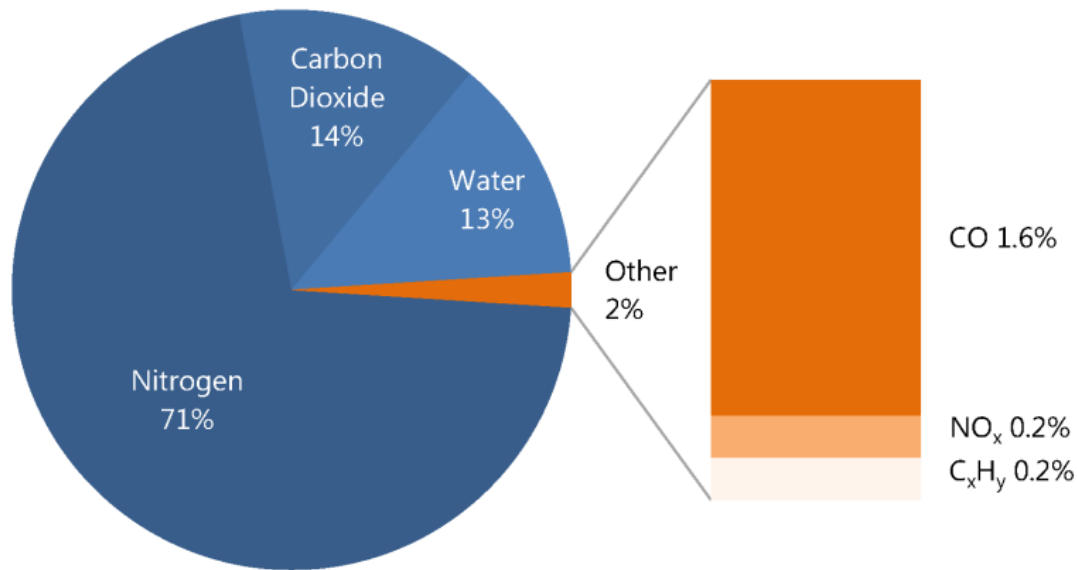


Figure 1.2: Average composition of exhaust gases from a gasoline vehicle [1]

amount of induced fresh air is not sufficient to completely burn all the fuel. Consequently, most of the hydrocarbon molecules begin the oxidation process up to the formation of CO , but then the further oxidation into CO_2 is inhibited by the lack of O_2 . To provide some figures, if $lambda (\lambda) = (A/F)/(A/F)_{st} = 0.9$ the expected average amount of CO at the exhaust is 3% v/v.

2. High temperature reached during the combustion process. The reaction rates are high enough to reach the chemical equilibrium, so that the reverse reaction starts to occur. This leads to the dissociation of CO_2 back into CO . Due to the subsequent temperature drop in the expansion stroke, the reactions freeze so that the concentration CO at the exhaust is higher than the corresponding equilibrium one. For this reason, even if $\lambda = 1$, the CO at the exhaust is around 1% v/v.

HC formation mechanisms

Unburnt hydrocarbons (HC) are the result of a partial fuel oxidation. Usually, about the 10% of fuel is not properly burned in the main combustion event due to several different phenomena, listed here for reference and whose importance depends on the engine operating conditions:

1. Trapping into crevices
2. Trapping into lubricant oil layer

3. Wall quenching
4. Bulk quenching
5. Accumulation in deposits

Fortunately, so-called post-flame oxidations occur during the expansion and exhaust strokes so that just 1% of the fuel injected will reach the ATS as HC.

NO_x formation mechanisms

Nitrogen oxides (*NO_x*) are produced when the temperature in the combustion chamber overcomes 1850 K and there is *O₂* available, but their appearance is not directly related to fuel oxidation. The main formation mechanism is in fact the thermal one, described by the Zeldovich reactions [2].

In particular, the term *NO_x* is used to refer to the sum of *NO* and *NO₂*.

For gasoline SI engines, the share of *NO_x* is about 98% *NO* and 2% *NO₂*. *NO_x* are more critical in the case of Diesel CI engines, being their working principle based on lean operation so that there is always an excess of *O₂*.

1.2 The Three-Way Catalyst

The Three-Way Catalyst, or Three-Way Catalytic Converter, (TWC) is the standard solution employed in the automotive industry to cut down tailpipe emissions of vehicles equipped with gasoline engines.

The term "Three-Way" reflects the capability of this device to simultaneously oxidize *CO* and *HC* into *CO₂* and to reduce *NO_x* into *N₂*. This is made possible by the employment of noble metals such as Platinum (Pt), Palladium (Pd) and Rhodium (Rh), also called Platinum Group Metals (PGM), that act as catalysts promoting the occurrence of the above mentioned reactions.

A generic chemical process involving the combination of certain reactant molecules into certain products can be expressed in the form:



The associated forward reaction rate can be represented by the following equation:

$$rate = k[A]^a[B]^b \quad \left[\frac{mol}{m^3s} \right] \quad (1.3)$$

Where [A] and [B] are the molar concentrations of the two reactant species.

The reaction rate constant "k" can be further written in the Arrhenius form:

$$k = Ae^{\left(-\frac{E_a}{RT}\right)} \quad (1.4)$$

Where:

- A: pre-exponent multiplier, adimensional
- Ea: activation energy in $\frac{J}{mol}$
- R: universal gas constant. $R = 8.314 \frac{J}{molK}$
- T: absolute temperature in Kelvin degree

From equation (1.4), it is straightforward to notice that the reaction rate constant increases with temperature, so does the reaction rate and thus the conversion efficiency, defined according to (1.5).

$$\eta = \frac{\dot{m}_{i,OUT} - \dot{m}_{i,IN}}{\dot{m}_{i,IN}} \quad (1.5)$$

Figure 1.3 shows the effect of temperature on TWC conversion efficiency:

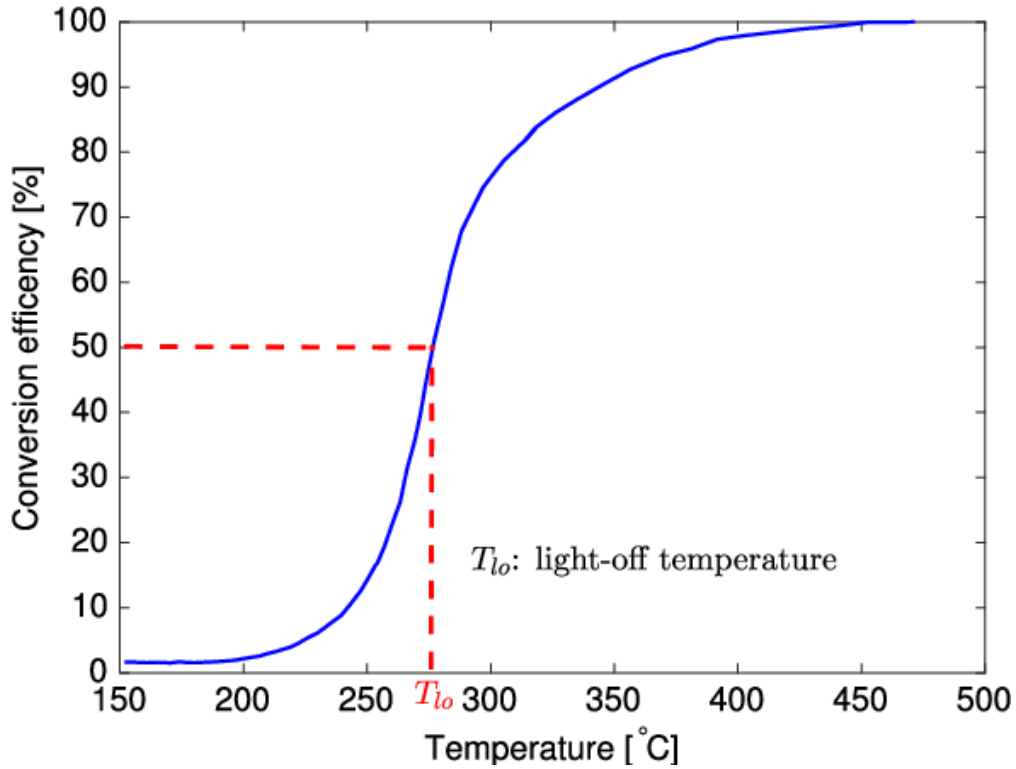


Figure 1.3: The effect of temperature on TWC conversion efficiency (Bresch-Pietri, Leroy, and Petit, 2013)

The ability of the PGM catalysts is to lower down the activation energy of the several oxidation and reduction processes occurring inside the TWC, without being

involved and consumed in the reactions. Thanks to this peculiar function, it is possible to obtain very high reaction rates even in the relatively low exhaust gas temperature range, thus cutting down drastically the tailpipe emissions. However, an essential requirement to maximize the reduction efficiencies for all the pollutant species is to let the engine to operate in a narrow window around stoichiometric conditions, as it is shown in figure 1.4:

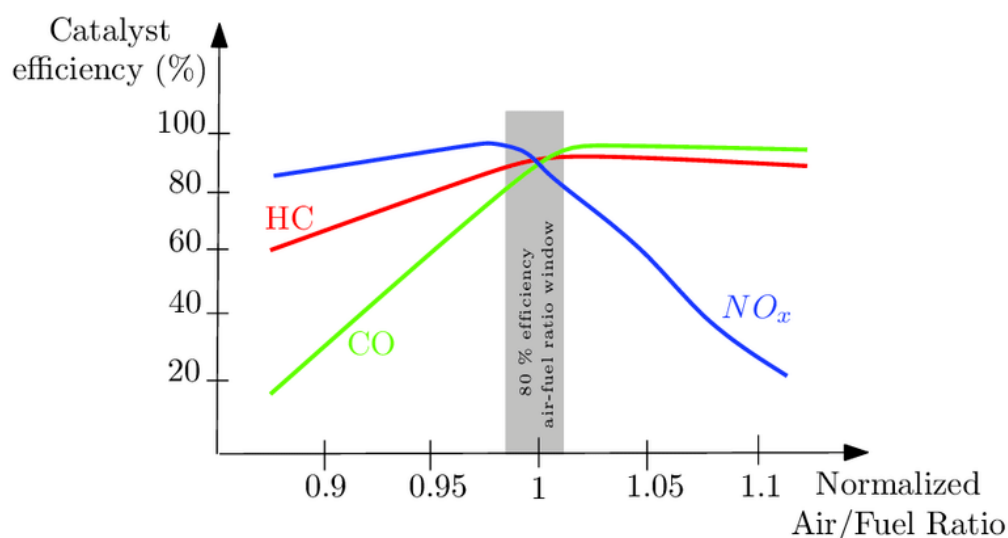
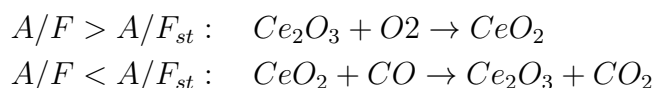


Figure 1.4: Three-Way Catalytic Converter Efficiency [3]

This is accomplished by the enforcement of a closed-loop control on the air/fuel ratio that exploits the signal coming from a Heated Exhaust Gas Oxygen (HEGO) sensor. Since λ oscillates around λ_{st} due to the HEGO sensor operation and engine working point, another metal element is present inside a TWC: Cerium. Cerium provides the so-called Oxygen Storage Capacity (OSC) thanks to its capability to easily form oxides. During lean operation, a share of the excess O_2 in the exhaust is stored in the form of trivalent Cerium Oxide, CeO_2 . The stored oxygen is then released during the rich operation phases, providing a fundamental support in the oxidation reactions. A simplified representation of the process is hereby reported:



In order to describe the actual physical and chemical processes behind the interaction of the exhaust stream with the PGM and Cerium, it is necessary to provide an overview of the structure of the device. Automotive TWCs belong to the category of heterogeneous flow-through monolith reactors.

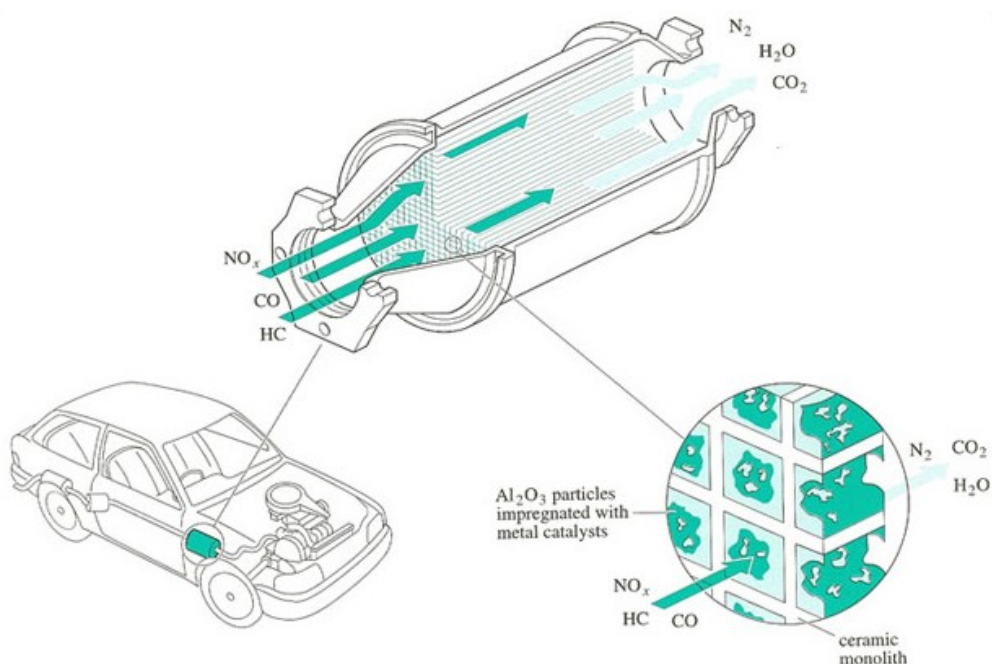


Figure 1.5: Schematic structure of a TWC [4]

Figure 1.5 allows to distinguish the following constituent element:

1. External canister
2. Substrate
3. Washcoat/Carrier
4. Catalytic active centers (PGM atoms)

The substrate is a ceramic or metallic honeycomb monolith constituted by hundreds of parallel channels that run all through from the inlet to the outlet. A washcoat layer, usually $\gamma - Al_2O_3$, is deposited on the walls of such channels. Finally, catalytic active centers (PGM atoms) are trapped on the washcoat surface during the manufacturing process. The use of $\gamma - Al_2O_3$ is justified by its high porosity, thanks to which it is possible to amplify by thousand of times the contact surface between gas and PGM atoms.

The complete conversion process of CO , HC and NO_x involves thus the following physical and chemical steps, schematized in figure 1.6:

1. Bulk (external) diffusion of reactants through the boundary layer towards the washcoat surface

2. Pore (internal) diffusion of reactants through washcoat pores
3. Adsorption of reactants on the active centers
4. Catalytic reaction
5. Desorption of products from the active centers
6. Pore (internal) diffusion of products through washcoat pores
7. Bulk (external) diffusion of products through the boundary layer towards the channel

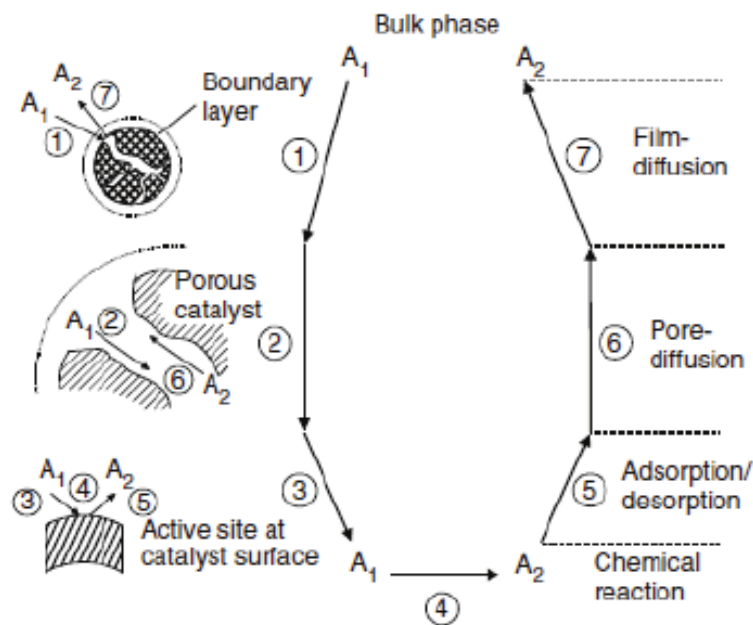


Figure 1.6: Individual steps of a simple, heterogeneous catalytic fluid–solid reaction $A_1 \rightarrow A_2$ carried out on a porous catalyst (Dittmeyer & Emig, 2008)

From this brief overview about TWC characteristics and operation, it is possible to appreciate the advantages behind its wide adoption as main emissions control system for gasoline vehicles [5]:

- It is a passive and relatively simple device
- It is designed to last for the entire life of the vehicle, rarely requiring maintenance
- It has negligible effects on fuel consumption

- It is relatively cheap, with much of the costs associated to the PGM loading

Unfortunately, TWCs suffer from a major disadvantage. Since the chemical kinetics strongly depends on temperature, the performances in terms of conversion efficiency are deeply impaired during cold start conditions. Moreover, TWCs are subjected to ageing phenomena associated with the gradual loss of catalytic active sites, so that the emissions abatement capabilities progressively reduce with the use of the vehicle.

1.3 1D Modelling and Calibration of TWC

Mono-dimensional (1D) numerical models play a fundamental role in the design and optimization of after-treatment systems. A reliable and accurate simulation tool is able to provide significant insight on the investigation of the best design choices from the early phases of development to the final optimization and setup of control strategies to fulfill legislation requirements. All this with relevant savings in terms of both time and costs compared to experimental campaigns.

In this context, the ultimate goal is to correctly reproduce the performances of the system in the wide range of real working conditions, characterized by large transients in temperature, exhaust mass flow and species concentration profiles.

Figure 1.7 shows the main phases of 1D after-treatment modelling and calibration process:

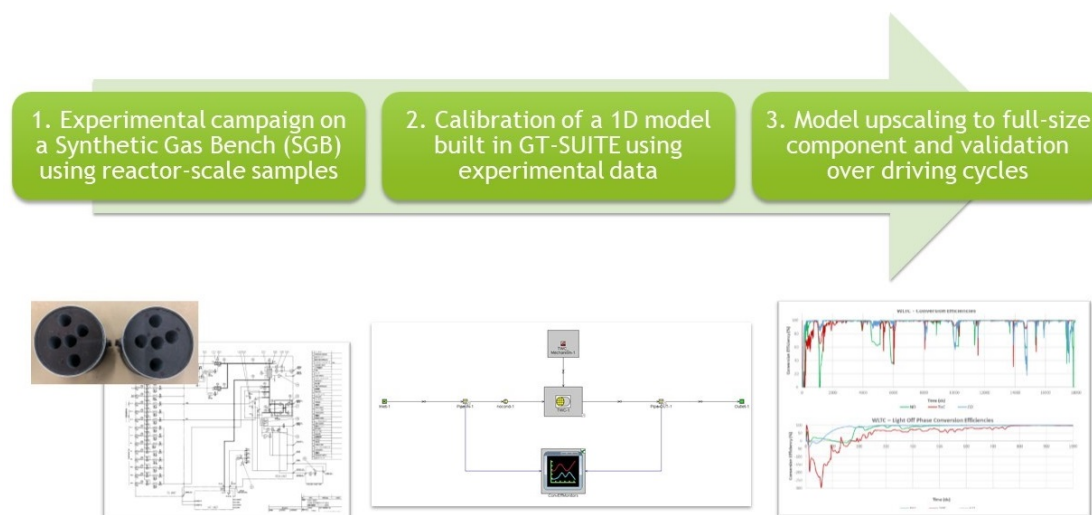


Figure 1.7: 1D ATS model development and calibration process [6]

The first step in the model development is to gain a comprehensive knowledge of the phenomena occurring in the device, especially for what concerns chemical

reactions and their kinetics. Currently, experimental campaigns are the only way to accomplish this task since, even if the physics behind the phenomena involved is well understood, no comprehensive predictive mathematical models have been developed yet.

The tests are usually conducted at the so-called Synthetic Gas Bench (SGB), figure 1.8, on catalyst core samples extracted from the full-size monolith.

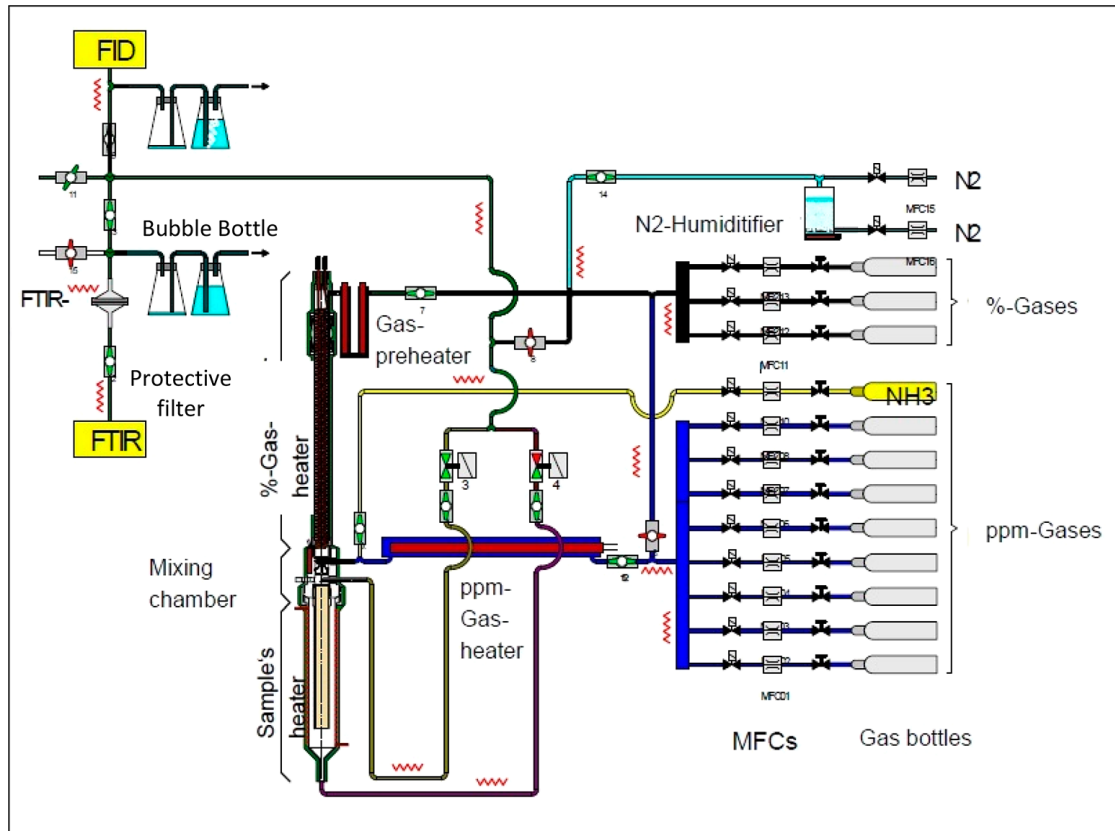


Figure 1.8: Schematic view of laboratory Synthetic Gas Bench [6]

SGB allows to accurately control the reactor inlet conditions in terms of temperature trace, mass flow rates and synthetic gas mixture composition, according to some pre-defined test protocols. Of course, these protocols are carefully chosen in conformity with the catalytic converter type and must be representative of the specific application. An example for TWC calibration is reported in table 1.1. Thanks to these features it is possible at first to separately investigate each reaction pathway and then to characterize the interactions among different species. Nevertheless, in the absence of availability of an SGB, it is anyway possible to characterize the device performances exploiting tailpipe emissions measurements collected at the chassis dynamometer.

Anyway, this method turns out to be much less effective in building a reliable model.

Characteristic	Test Protocol
Oxygen Storage Capacity	Lean/rich cycling phases at constant temperature to investigate oxygen storage during lean phases and CO and HC oxidation during rich phases
Light-Off	With constant inlet species concentration, a temperature ramp from 100°C to 500°C, with a rate of 5°C/min, is applied to characterize CO and HC oxidation and NO reduction

Table 1.1: Test protocol to characterize TWC operation by means of SGB experiments

The experimental data obtained are subsequently exploited to identify the set of reactions defining the mechanism and to calibrate the related kinetics parameters using proper strategies and optimization tools.

Three different approaches can be actually found in literature for the definition of the catalyst kinetics scheme in the simulation environment:

1. Maps/Look-up tables (obsolete)
2. Global reactions
3. Micro-kinetics

"With a micro kinetics approach, all the reactions sub-steps are detailed and modeled, which often requires a significant calibration effort, due to the large number of variables involved, and a deep understanding of the kinetics, which could be only obtained by means of an extensive laboratory-scale characterization. A global kinetic approach instead does not consider all the elementary steps behind each reaction, thus reducing the calibration effort required and the complexity of the problem" (1D simulation models for aftertreatment components, Millo, Federico; Gundlapally, Santhosh; Wang, Wen; Syed Wahiduzzaman, 2020, pp. 406).

For the above mentioned reasons, the most commonly adopted method by the ATS modelling community, and the chosen one for this activity, consists in the use of global reaction schemes.

The usual way to proceed is to select, from similar literature works, an existing scheme that fits the needs, and to implement the necessary modifications if required.

The calibration is a sequential process that follows the evolution of the experimental campaign, from the investigation of the single reactions to the evaluation of the interactions among species.

The parameters targeted by the optimization belong to the following classes:

1. PGM and Cerium Dispersion Factors
2. Pre-exponentials: “ A_i ”
3. Activation energies: “ Ea_i ”
4. Inhibition functions: “ G_j ”

For each step of the calibration, it is fundamental to isolate the most relevant independent variables in order to reduce as much as possible their number, thus simplifying the optimization problem.

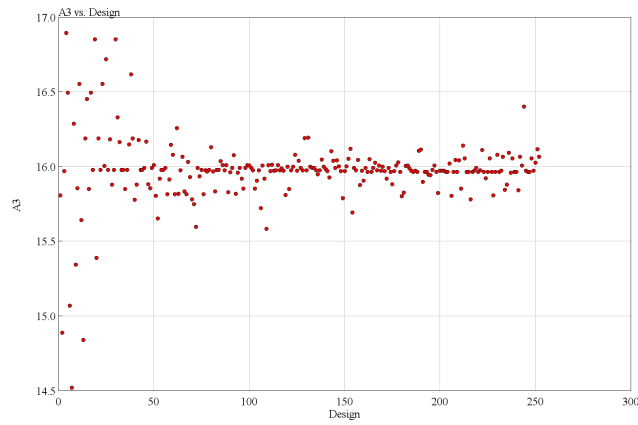
Among the several optimization tools available, the choice for the present work is to exploit the Genetic Algorithm (GA) embedded in the simulation software, GT-SUITE, according to what presented in [7]. A great advantage in the use of this algorithm is that the user is not expected to have a deep understanding of the chemistry. Its goal is to minimize an objective function that evaluates the difference between the measured and the simulated outlet species concentrations. The setup of the GA requires the definition of the number of generations and the related population. The population is composed of individuals, which are vectors representing a combination of calibration parameters. The total number of design is given by equation (1.6):

$$total \# \text{ of designs} = (\# \text{ of generations}) * (\text{population size}) \quad (1.6)$$

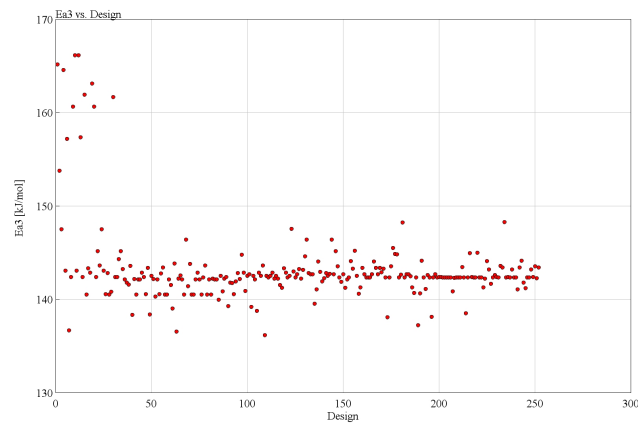
The GA optimization starts with the random choice of the values for the individuals of the population of the first generation. The values are taken inside the range specified by the user. After the simulation of the entire first generation, the fitness of each individual is evaluated based on the objective function. The individuals that lead to the lowest error are then selected and used to evolve the population for the next generation, up to the last.

An example of the expected outcome of a successful two-parameters optimization is showed in figure 1.9, where it can be observed how the independent variables and the objective function evolve up to converging to their optimum.

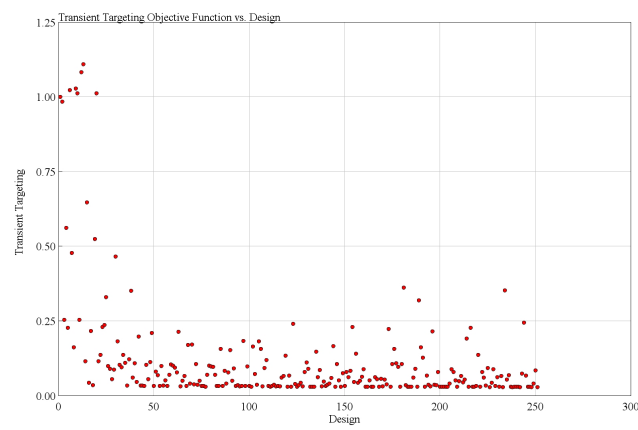
Once the calibration of the reactor-scale model is completed, in principle it would be possible to transfer the kinetics scheme to the full-size component without any modifications and then to perform the validation over different driving cycles.



(a) Evolution of parameter #1 throughout the iterations



(b) Evolution of parameter #2 throughout the iterations



(c) Evolution of the objective function throughout the iterations

Figure 1.9: Example of GA output for a two-parameters optimization

However, literature shows that deviations in simulation predictions are observed when performing the up-scaling. The main reason for this is that a very small number of representative HC, usually just two or three, is employed during SGB experiments and consequently modeled, while a real exhaust gas stream includes a large variety of HC species. Moreover, heat and mass transfers occurring in the full-size component become important if compared to the laboratory-scale sample, that is subjected to controlled inlet conditions [8].

Chapter 2

Experimental Characterization on Synthetic Gas Bench (SGB)

The after-treatment system under analysis belongs to an high performance gasoline engine and consists of two parallel lines connected to two banks of cylinders. Each line includes a TWC in close-coupled configuration and a coated Gasoline Particulate Filter (cGPF).

This modelling and calibration activity is focused on the TWC device, whose main specifications are showed in table 2.1.

The amount of Cerium and PGM loading are omitted for confidentiality reasons.

Specification	Value
diameter [mm]	127
length [mm]	90
Substrate material	Stainless steel
Cell density [cpsi]	800
Substrate wall thickness [μm]	40
PGM loading	Pd and Rh

Table 2.1: TWC specifications

2.1 Experimental Set-Up

The experimental characterization has been conducted by the REACT laboratory of the Queen's University of Belfast on samples of both right and left banks, provided by Ferrari S.p.A. The catalysts have been dismantled from the exhaust line of a vehicle having a mileage of 5000 km. In particular, several cores have been drilled from the full-size monoliths in order to perform a preliminary evaluation of in-brick and bank-to-bank differences in performances (figure 2.1). Each core has a diameter of 25 mm and a length of 90 mm.

Since no relevant deviation has been observed from the above mentioned comparison, the entire experimental campaign focused on the central core of the left bank (core C highlighted in green in figure 2.1).

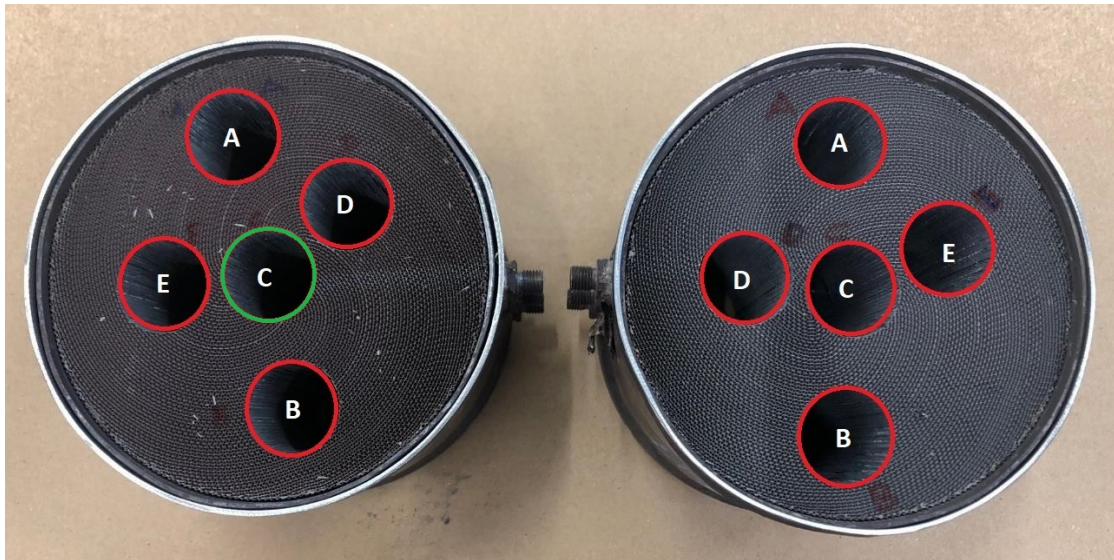


Figure 2.1: Left and Right bank monoliths with core locations

The OSC behaviour, the conversion efficiencies and their dependence on temperature have been investigated using an Horiba SIGU SGB according to properly defined test protocols. Such kind of tests involve the use of gas species representative of those present in a gasoline SI exhaust environment. The broad range of test strategies, employing varying gas concentrations, temperature profiles and test conditions, provided the necessary data for the calibration of the kinetic expressions used in the simulation software.

The catalyst core is placed inside a reactor equipped with a pre-heating quartz tube and inserted into a furnace (figure 2.2).

Inlet and outlet catalyst temperatures have been measured by two k-type thermocouples, $d=1.6$ mm, placed respectively ~ 2 mm in front of and from the rear of

the centre of the catalyst core inlet and outlet faces. Inlet species concentrations and mass flow rates are controlled by the built-in mass flow controllers (MFC) of the Horiba SIGU according to their nominal values. Outlet species concentrations are recorded by an Horiba 6000FT (Fourier Transform Infra-Red Spectroscopy Analyser, FTIR) which is capable of a wide range of compound speciation, i.e. CO , C_3H_6 [ppmC3], NO , NO_2 , N_2O , NH_3 , CO_2 , H_2O . In addition, THC [ppmC1] and O_2 concentrations are logged from an Horiba EXSA five-gas analyser. C_3H_8 outlet concentrations are computed from the measurements of THC and C_3H_6 . Finally, inlet and outlet λ measurements are provided by two λ sensors.



Figure 2.2: Reactor unit with pre-heating quartz tube removed from furnace and mixing plate exposed

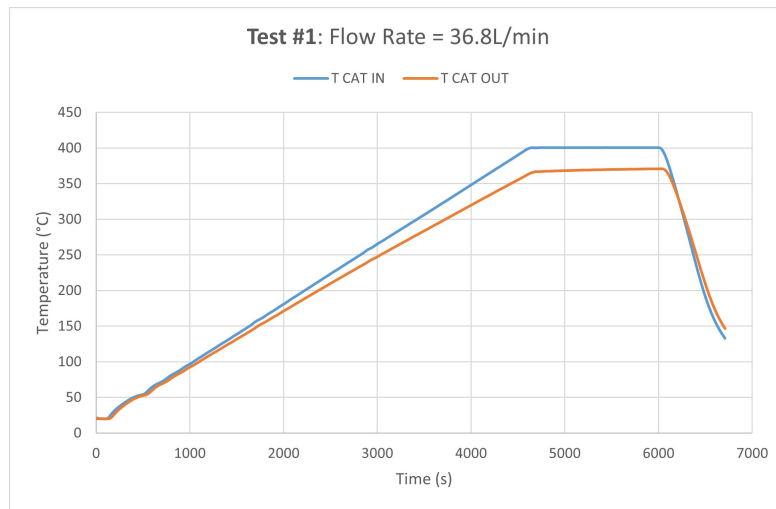
Test types includes:

1. Warm-up tests, to evaluate the heat losses in the reactor
2. OSC tests, under isothermal conditions at three temperature levels

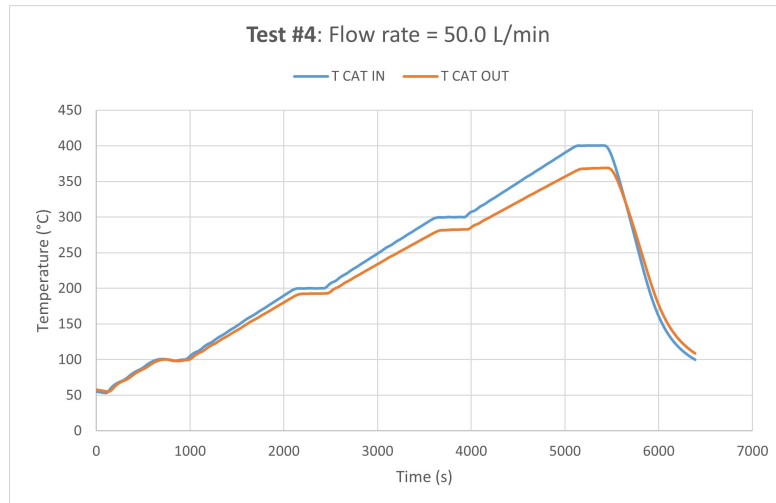
- Light-Off tests, ranging from the investigation of single reactions to the feeding of the full gas mixture

2.1.1 Warm-Up Tests

Warm-up tests involved the evaluation of the heat losses occurring in the reactor. As described in paragraph 1.2, temperature plays a key role in chemical kinetics thus it is fundamental to evaluate the thermal behavior of the system to correctly replicate it in the simulation model.



(a) T Ramp #1



(b) T Ramp #4

Figure 2.3: Inlet and outlet core temperatures traces for tests #1 & #4

The features of these tests are listed below:

- N_2 only as inlet species. This choice avoids the occurrence of any reaction, being N_2 an inert gas
- Two representative flow rates: 36.8 L/min and 50 L/min, corresponding to a Gas Hourly Space Velocity (GHSV) of $50000\ h^{-1}$ and $67935\ h^{-1}$ respectively
- Five representative temperature ramps up to 400°C , with a rate of $5^\circ\text{C}/\text{min}$

The results of two out of the five tests are reported in the charts included in figure 2.3. During the constant T phase at 400°C , a delta of $\sim 35^\circ\text{C}$ between inlet and outlet core sections is observed for all the tests.

2.1.2 OSC Tests

Oxygen Storage tests aimed at investigating the O_2 storage in the form of Ceria oxides during lean phases and the subsequent O_2 depletion in the oxidation of CO and HC during rich phases.

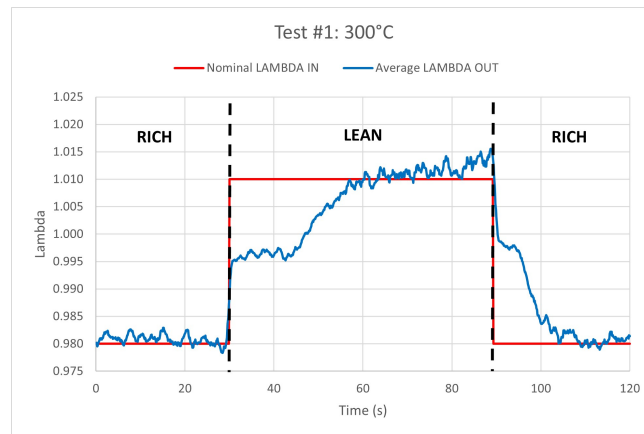
In particular, the test strategy focused on oxygen capacity measurements, identification of the reactions to be included in the model and their temperature-dependent kinetics.

To simulate the perturbation of the air-to-fuel ratio in an engine, the SIGU utilizes an assembly comprised of four automotive injectors. Two injectors are for lean mixture delivery and two are for rich mixture delivery. These injectors are located as close as physically possible to the reactor inlet in order to achieve rapid switching. Test protocol specifications:

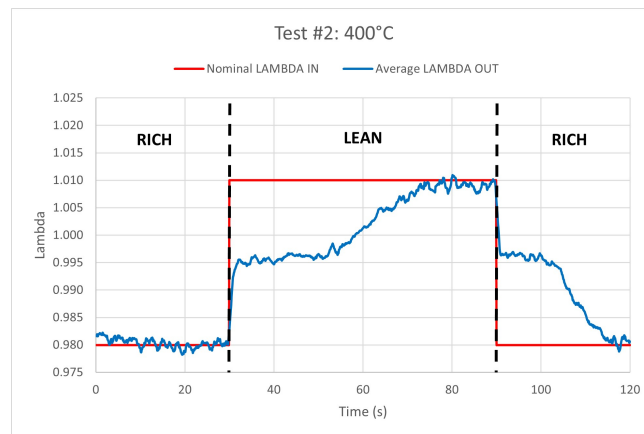
- Flow Rate = 36.8L/min, equating to a GHSV = $50,000\ h^{-1}$ and Mass Flow Rate = 2.761 kg/h
- Lean Gas Mixture = 0.25% O_2 in N_2 for 60s ($\lambda = 1.01$)
- Rich Gas Mixture = 1.0% CO in N_2 for 60s ($\lambda = 0.98$)
- The inlet temperature was held constant at the desired setpoints which were 300, 400 and 500°C

Due to the rapid nature of the oxygen storage response, the oxygen measurement provided by the paramagnetic analyser in the Horiba EXSA five-gas analyser could not achieve the necessary resolution. As such, a lambda sensor was fitted in the most practical position within the SIGU which is on the heated outlet sampling line.

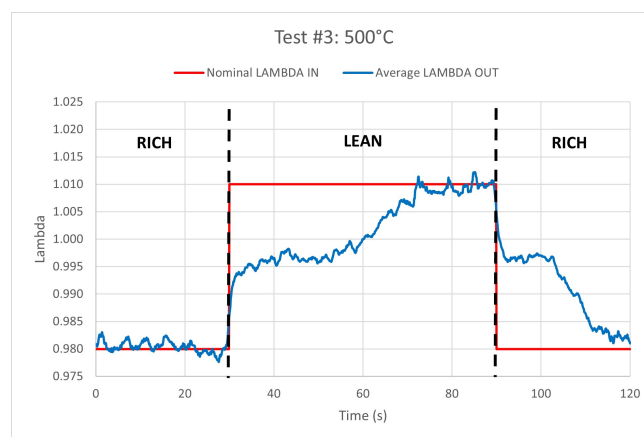
Figure 2.4 provides the measurements of this lambda sensor for the three isothermal tests:



(a)



(b)



(c)

Figure 2.4: Inlet and outlet λ measurements from the three isothermal OSC tests

From the 300°C condition to 400°C one, there is an evident shift in the filling characteristic of the OSC. On the contrary, very little differences are present between the 400°C and 500°C tests. This is further highlighted in table 2.2 which reports the average delays to get $\lambda=1.01$ at the catalyst outlet after the beginning of the lean phase.

Test ID	Average Time
Test #1: 300°C	26.8 s
Test #2: 400°C	41.1 s
Test #3: 500°C	40.4 s

Table 2.2: Rich-to-lean average time to get $\lambda = 1.01$

2.1.3 Light-Off Tests

Light-off tests are fundamental to investigate the oxidation and reduction reactions occurring in the device and to gain the required knowledge on their kinetics, that once again is primarily dependent on the temperature.

A first set of tests has been carried out to evaluate the overall performances of the catalyst when a gas mixture representative of the real vehicle exhaust gas is fed to the reactor. These tests have been used for the final model validation. From now on, they will be referred to as "full mixture performance testing".

Subsequently, several test protocols have been defined to separately analyze each reaction, at first considering the conversion of one pollutant at a time, and then feeding more complex mixtures to characterize all the possible interactions among species. These tests have been used to calibrate the kinetics scheme. From now on, they will be referred to as "simplified mixture detailed testing".

The choice of the concentrations of the different species has been made considering the average engine-out emissions measured on the chassis dynamometer over the New European Driving Cycle (NEDC) [9], World Harmonized Light-Duty Test Cycle (WLTC) [10] and the EPA Federal test Procedure (FTP75) [11] driving cycles, reported in table 2.3.

<i>CO</i> (%)	<i>THC</i> (ppmC1)	<i>NO</i> (ppm)	<i>CO₂</i> (ppm)	<i>H₂O</i> (%)
1.0	836	775	12.4	10.7

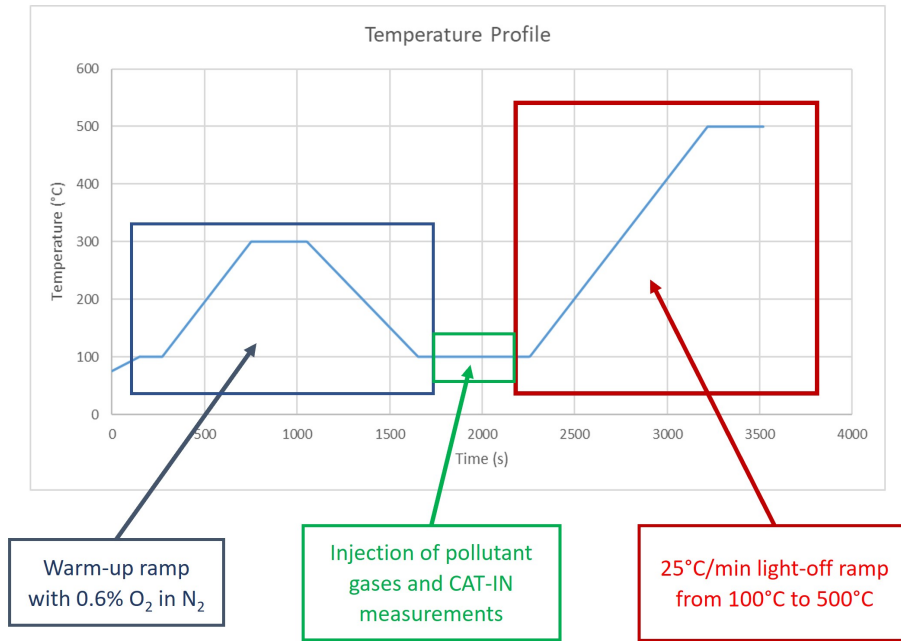
Table 2.3: Average engine-out emissions over NEDC, WLTC and FTP75 driving cycles

The test conditions for the two sets of tests are listed in what follows:

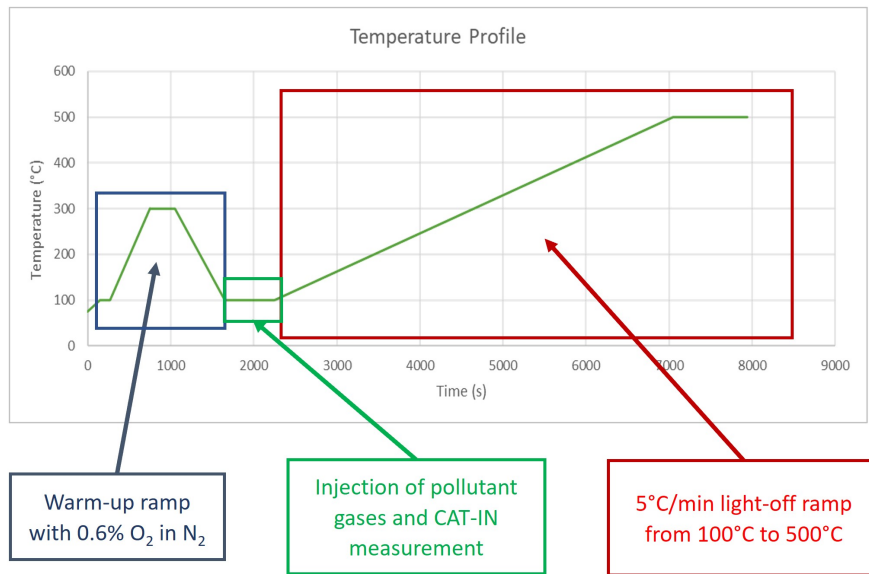
- Flow Rate = 36.8L/min, equating to a GHSV = 50,000 h^{-1} and Mass Flow Rate = 2.761 kg/h
- All gases are controlled at a steady flow rate by the built-in mass flow controllers of the SIGU
- The gas mixtures used for performance testing can be seen in table 2.4. The gas mixtures used for detailed testing vary from test to test and can be seen in table 2.6. The THC feed is made up of 600 ppmC1 of C_3H_6 and 450 ppmC1 of C_3H_8 , a reasonable way out to represent the HC in the exhaust of a gasoline engine
- The tests begin with a warm-up temperature ramp up to 300°C, during which only N_2 and 0.6% O_2 are fed to the sample. The purpose of this initial phase is to ensure a consistent temperature profile of the reactor for each test and to oxygenate the Ceria sites to have full storage for the subsequent light-off phase
- The pollutant gases are turned on when the inlet temperature is steady at 100°C. At that point, a pre-cat measurement is taken to ensure that the actual inlet concentrations are close enough to the nominal values
- The temperature ramp used is 25°C/min for performance testing (figure 2.5 (a)) and 5°C/min for detailed testing (figure 2.5 (b)), starting from 100°C to a maximum of 500°C where the temperature is held steady for 5 minutes before it is left free to decrease

CO (%)	THC (ppmC1)	NO (ppm)	CO_2 (ppm)	H_2O (%)
1.5	1050	1000	14	5

Table 2.4: SGB light-off full mixture composition for performance testing

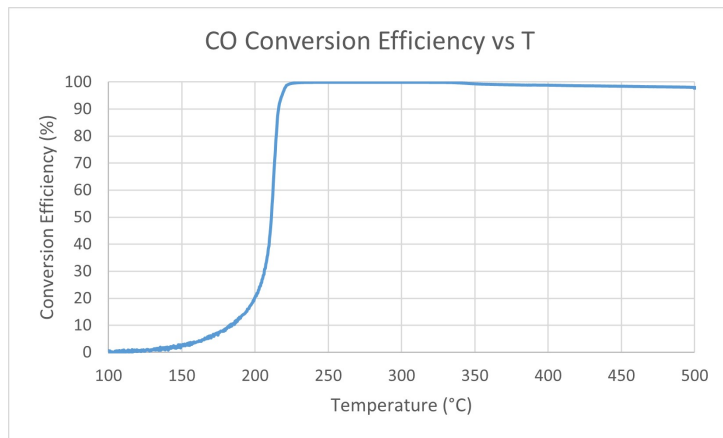


(a) Test protocol for performance tests

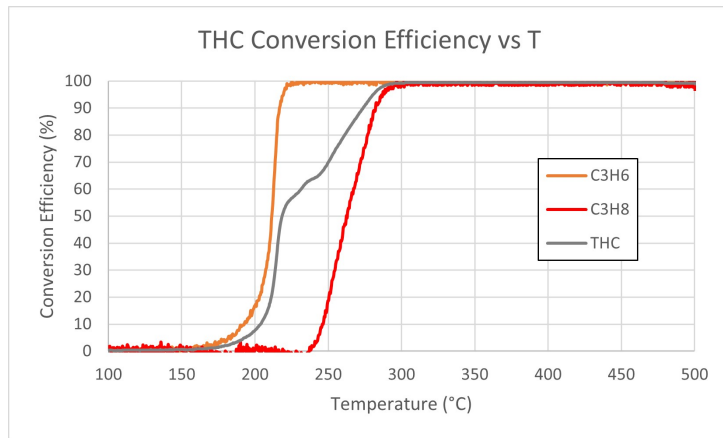


(b) Test protocol for detailed tests

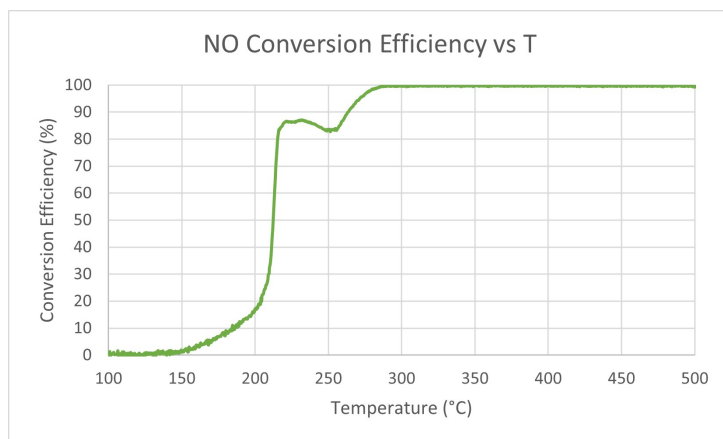
Figure 2.5: Light-off Tests protocols



(a)



(b)



(c)

Figure 2.6: Light-off Full Mixture Performance Test

The results of the full mixture performance testing are showed in figure 2.6. It is possible to observe that CO and C_3H_6 undergo a rapid and smooth full conversion after a certain threshold temperature is reached. The NO is instead subjected to a stall in the high conversion region around 85%. Furthermore, it is evident how the subsequent achievement of the 100% conversion is strictly related to the C_3H_8 oxidation.

Table 2.5 summarizes the results in terms of T10s, T50s, T90s, i.e. the light-off temperatures associated to the achievement of, respectively, 10%, 50% and 90% of conversion efficiency.

Species	Light-Off Temperatures		
	T10s (°C)	T50s (°C)	T90s (°C)
CO	185	211	216
C_3H_6	193	212	217
THC	204	219	274
NO	186	213	264

Table 2.5: Performance testing - CO , C_3H_6 , THC , NO light-off temperatures

Test ID #	CO [ppm]	C_3H_6 [ppmC3]	C_3H_8 [ppmC3]	NO [ppm]	O_2 [ppm]	H_2O [%]
1	15000	-	-	-	7500	-
2	-	200	-	-	900	-
3	-	-	150	-	750	-
4	15000	200	150	-	9150	-
5	15000	-	-	-	-	5
6	15000	-	-	-	7500	5
7	15000	200	150	-	9150	5
8	1500	-	-	1500	200	-
9	-	200	-	1000	200	-
10	-	-	150	1000	-	-

Table 2.6: Gas mixture compositions for light-off detailed testing. Balanced N_2

An example of light-off detailed test outcome using the inlet composition of test #1 is depicted in figure 2.7. After the initial warm-up phase during which only O_2 and N_2 are present, the feed of CO is initiated. CO is oxidized into CO_2 with stoichiometric O_2 , so that after 4000s its outlet concentration drops down to zero. During the final cooling phase, the CO conversion is maintained to a lower inlet temperature than during light-off.

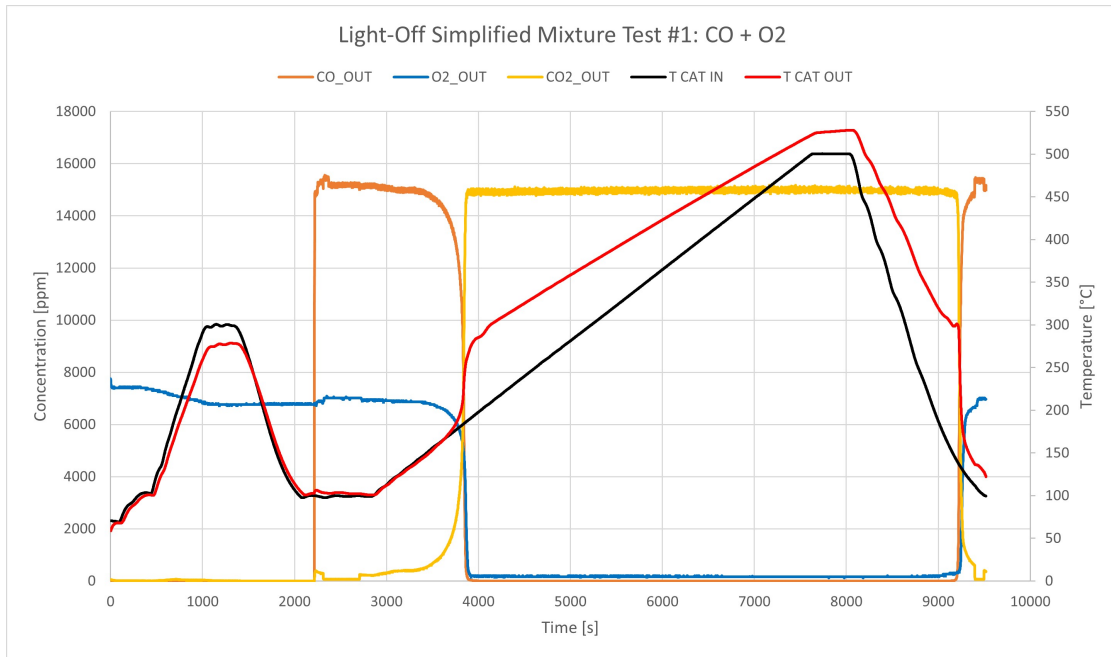


Figure 2.7: Light-off Simplified Mixture Detailed Test #1: $CO + O_2$

This is a common situation experienced in all the tests. The reason for this asymmetric behavior during the light-off is that the monolith temperature is kept high by the heat produced by the ongoing exothermic reaction, as it can be seen looking at the T CAT OUT trace.

Chapter 3

Model Development and Calibration

The data collected during the experimental campaign reviewed in Chapter 2 have been used to calibrate the global kinetics model of the TWC. This model was built utilizing a one-dimensional (1D) multi-physics fluid-dynamic code, GT-SUITE. The optimization tool employed was the Genetic Algorithm embedded in the software, that turned out to be successful and fast in finding the optimal values for all the parameters of the calibration.

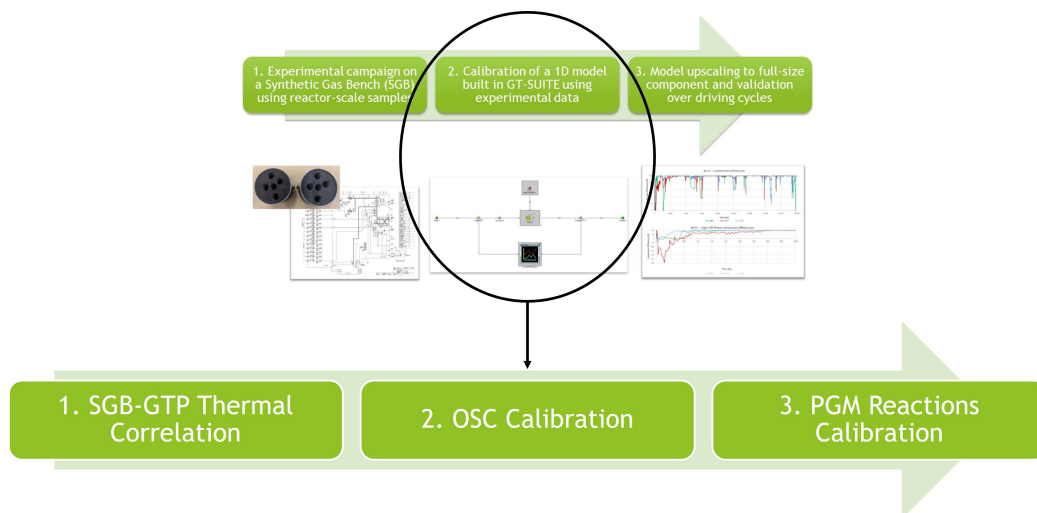


Figure 3.1: 1D reactor-scale TWC model calibration process

The calibration process began with a thermal correlation, necessary to correctly reproduce the heat losses occurring in the reactor. Then, the OSC behavior was

optimized, followed by the calibration of the PGM reactions, including the oxidation and reduction ones. The flowchart of the process can be seen in figure 3.1.

The kinetics scheme has been defined starting from the one presented by Ramanathan & Sharma [12], which includes 15 reactions. From now on, this scheme will be referred to as "**Baseline 1**". To this scheme, five reverse reactions occurring on Ceria sites were added, for a total of 20 reactions. The same kinetics scheme, but calibrated by Ferrari exploiting real tailpipe emissions, was used as a benchmark to appreciate the improvements introduced by the calibration activity. From now on, this scheme will be referred to as "**Baseline 2**".

Being that a stand-alone reactor-scale TWC device was analysed, and not an entire exhaust line, the model looks quite simple, as it can be seen in figure 3.2. Inlet conditions, in terms of mass flow rates, species concentrations and temperature profiles, are defined in part #1. Two short pipelines, parts #2, connect the upstream and downstream environments to the inlet and outlet catalyst pipes, parts #3, in which are embedded the thermocouple models for gas temperature measurements. Part #4 is used to model the geometrical and material properties of the TWC, while the chemical reactions are defined in part #5.

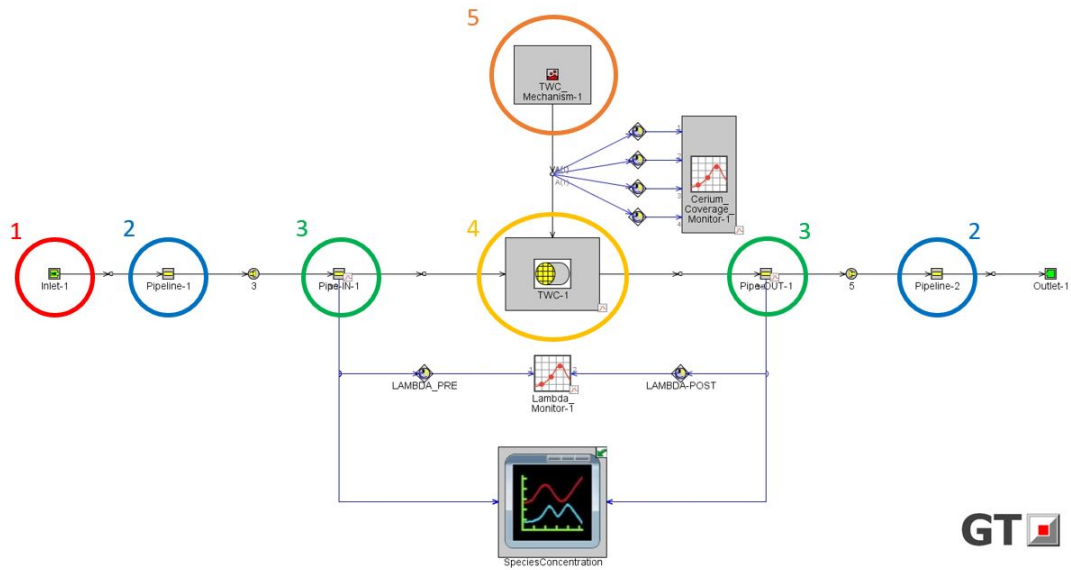


Figure 3.2: 1D CFD model of reactor-scale TWC built in GT-SUITE v2020

3.1 Kinetics Scheme Definition

The global reaction scheme defined for the TWC model is reported in table 3.1. It includes *CO* and *HC* oxidation reactions on Pd sites (PGM1) and *NO* reductions

on Rh sites (PGM2), as well as oxygen storage and depletion on Ceria sites. The reactions in bold, i.e. reactions #12, #13, #14, #19 and #20, are the reverse Ceria reactions added to the baseline scheme by Ramanathan & Sharma [12].

Reaction rates have been expressed in Arrhenius form according to what presented in section 1.2:

$$R_i = k_i * \{conc\} * A(y)/G_j \quad (3.1)$$

Where:

$$k_i = A_i * e^{\left(-\frac{E_{a_i}}{RT}\right)} \quad (3.2)$$

Looking at equation (3.1) it is possible to notice that two additional terms have been included in the reaction rate expression:

- $A(y)$: coverage expressions. Used for storage sites like Cerium, that can assume two different forms: CeO_2 & Ce_2O_3 . The coverage represents the fraction of storage element available in a specific form. Correspondingly, in the case of Cerium, $A(Ce_2O_3) = 1 - A(CeO_2)$
- G_j : inhibition functions (equation (3.3)). Defined to take into account the competition among pollutant species whose oxidation and reduction reactions are catalyzed on the same PGM site. Popularized by Voltz et al. (1973), and continued by Oh and Cavendish (1982). Accordingly, one inhibition function has been defined for Pd (G_1) and one for Rh (G_3) sites.

$$G_j = (1 + k_{ja} * [CO] + k_{jb} * [C_3H_6])^2 + \left(1 + k_{jc} * [CO]^2 * [C_3H_6]^2 + (1 + k_{jd} * [NO])\right) \quad (3.3)$$

Where:

$$k_{jm} = A_{jm} * e^{\left(\frac{-E_{a_{jm}}}{R*T}\right)} \quad \text{with } m = a, b, c, d \quad (3.4)$$

The reaction rate expressions for each reaction reported in table 3.1 are listed in table 3.2. The chosen rate expression basis had associated units of moles per second per moles of active sites. This choice led to a kinetics scheme that is independent from the geometrical properties of the device, so easily portable on similar models. The rate expression is internally multiplied by the active site density of its associated site element, resulting in units of moles per second per reactor volume. The active site density is computed according to equation (3.5):

$$Active\ Site\ Density = \frac{Loading\ of\ Site\ Element * Dispersion\ Factor}{Atomic\ Weight} \quad (3.5)$$

The dispersion factor represents the ratio of active sites to total sites, that is how much of the theoretical site element loading is actually available to react.

#	Site	Reaction
1	PGM1	$CO + 0.5O_2 \rightarrow CO_2$
2	PGM1	$C_3H_6 + 4.5O_2 \rightarrow 3CO_2 + 3H_2O$
3	PGM1	$C_3H_8 + 5O_2 \rightarrow 3CO_2 + 4H_2O$
4	PGM1	$H_2 + 0.5O_2 \rightarrow H_2O$
5	PGM2	$CO + NO \rightarrow CO_2 + 0.5N_2$
6	PGM2	$C_3H_6 + 9NO \rightarrow 3CO_2 + 3H_2O + 4.5N_2$
7	PGM2	$H_2 + NO \rightarrow H_2O + 0.5N_2$
8	PGM1	$CO + H_2O \rightarrow CO_2 + H_2$
9	PGM1	$C_3H_6 + 3H_2O \rightarrow 3CO + 6H_2$
10	Cerium	$2Ce_2O_3 + O_2 \rightarrow 4CeO_2$
11	Cerium	$Ce_2O_3 + NO \rightarrow 2CeO_2 + 0.5N_2$
12	Cerium	$Ce_2O_3 + H_2O \rightarrow H_2 + 2CeO_2$
13	Cerium	$Ce_2O_3 + CO_2 \rightarrow CO + 2CeO_2$
14	Cerium	$6Ce_2O_3 + 3CO + 3H_2O \rightarrow C_3H_6 + 12CeO_2$
15	Cerium	$CO + 2CeO_2 \rightarrow Ce_2O_3 + CO_2$
16	Cerium	$C_3H_6 + 12CeO_2 \rightarrow 6Ce_2O_3 + 3CO + 3H_2O$
17	Cerium	$C_3H_8 + 14CeO_2 \rightarrow 7Ce_2O_3 + 3CO + 4H_2O$
18	Cerium	$H_2 + 2CeO_2 \rightarrow Ce_2O_3 + H_2O$
19	Cerium	$4CeO_2 \rightarrow 2Ce_2O_3 + O_2$
20	Cerium	$2CeO_2 + 0.5N_2 \rightarrow Ce_2O_3 + NO$

Table 3.1: TWC global reactions scheme [12]

This can be used to account for reduced activity due to ageing, poisoning, or general deactivation of sites [13].

The term G_2 in reaction rate #8 represents the water-gas shift (WGS) equilibrium constant [14], defined as:

$$G_2 = \exp\left(-\frac{(-41034 + 44.19 * T - 0.005553 * T^2)}{RT}\right) \quad (3.6)$$

The parameters (independent variables) targeted by the optimization belong to the following classes:

1. PGM and Cerium Dispersion Factors
2. Pre-exponentials: “ A_i ”
3. Activation energies: “ Ea_i ”
4. Inhibition functions: “ G_j ”

#	Site	Reaction Rate
1	PGM1	$R_1 = A_1 e^{-\frac{Ea_1}{RT}} C_{CO} C_{O_2} / G_1$
2	PGM1	$R_2 = A_2 e^{-\frac{Ea_2}{RT}} C_{C_3H_6} C_{O_2} / G_1$
3	PGM1	$R_3 = A_3 e^{-\frac{Ea_3}{RT}} C_{C_3H_8} C_{O_2} / G_1$
4	PGM1	$R_4 = A_4 e^{-\frac{Ea_4}{RT}} C_{H_2} C_{O_2} / G_1$
5	PGM2	$R_5 = A_5 e^{-\frac{Ea_5}{RT}} C_{CO} C_{NO} / G_3$
6	PGM2	$R_6 = A_6 e^{-\frac{Ea_6}{RT}} C_{C_3H_6} C_{NO} / G_3$
7	PGM2	$R_7 = A_7 e^{-\frac{Ea_7}{RT}} C_{H_2} C_{NO} / G_3$
8	PGM1	$R_8 = A_8 e^{-\frac{Ea_8}{RT}} [C_{CO} C_{H_2O} - C_{H_2} C_{CO_2}] / G_1 / G_2$
9	PGM1	$R_9 = A_9 e^{-\frac{Ea_9}{RT}} C_{C_3H_6} C_{H_2O} / G_1$
10	Cerium	$R_{10} = A_{10} e^{-\frac{Ea_{10}}{RT}} C_{O_2} A(Ce_2O_3)$
11	Cerium	$R_{11} = A_{11} e^{-\frac{Ea_{11}}{RT}} C_{NO} A(Ce_2O_3)$
12	Cerium	$\mathbf{R}_{12} = \mathbf{A}_{12} e^{-\frac{Ea_{12}}{RT}} C_{H_2O} \mathbf{A}(Ce_2O_3)$
13	Cerium	$\mathbf{R}_{13} = \mathbf{A}_{13} e^{-\frac{Ea_{13}}{RT}} C_{CO_2} \mathbf{A}(Ce_2O_3)$
14	Cerium	$\mathbf{R}_{14} = \mathbf{A}_{14} e^{-\frac{Ea_{14}}{RT}} C_{CO} C_{H_2O} \mathbf{A}(Ce_2O_3)$
15	Cerium	$R_{15} = A_{15} e^{-\frac{Ea_{15}}{RT}} C_{CO} A(CeO_2)$
16	Cerium	$R_{16} = A_{16} e^{-\frac{Ea_{16}}{RT}} C_{C_3H_6} A(CeO_2)$
17	Cerium	$R_{17} = A_{17} e^{-\frac{Ea_{17}}{RT}} C_{C_3H_8} A(CeO_2)$
18	Cerium	$R_{18} = A_{18} e^{-\frac{Ea_{18}}{RT}} C_{H_2} A(CeO_2)$
19	Cerium	$\mathbf{R}_{19} = \mathbf{A}_{19} e^{-\frac{Ea_{19}}{RT}} \mathbf{A}(CeO_2)$
20	Cerium	$\mathbf{R}_{20} = \mathbf{A}_{20} e^{-\frac{Ea_{20}}{RT}} C_{NO} \mathbf{A}(CeO_2)$

Table 3.2: Reaction rates expressions

3.2 Thermal Correlation

The thermal behavior was calibrated exploiting the five warm-up tests reviewed in section 2.1.1. The goal of this first step was to let the simulation being able to predict the heat losses and the thermal inertia observed in the experimental setup. To accomplish this task, the geometric and thermal properties of superwool insulation and reactor holder have been implemented in the model as outer catalyst layers, together with the substrate and washcoat properties of the TWC. The measured temperature profile by the thermocouple at core inlet (T CAT IN) was used as input temperature trace for the simulation. All the reactions were deactivated since only N_2 was fed at the inlet.

The outlet catalyst temperature (T CAT OUT) from the simulation was found out to be affected by:

1. TWC discretization length & solver master time step
2. Inlet pipe wall temperature method
3. Upstream TWC orifice type
4. Thermocouple emissivity

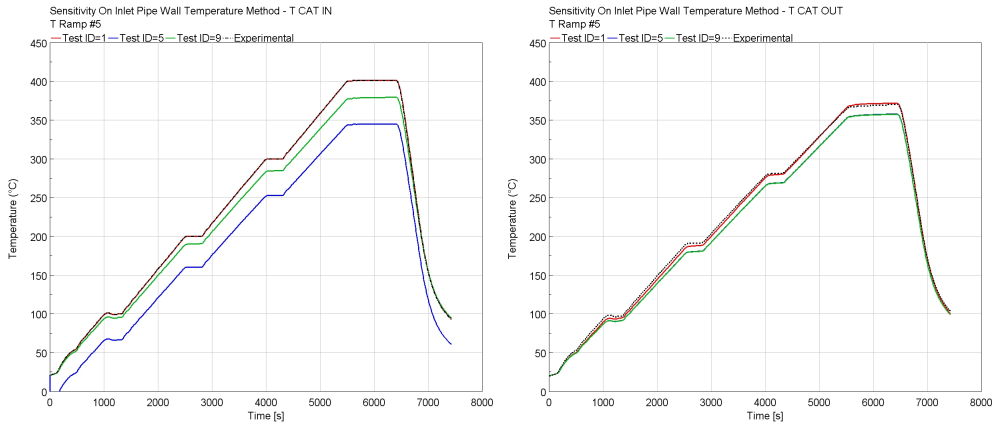
# test	Inlet pipe wall T method	Upstream TWC orifice type	Thermocouple emissivity
1	imposed	def	0.28
2	imposed	def	0
3	imposed	nocond	0.28
4	imposed	nocond	0
5	adiabatic	def	0.28
6	adiabatic	def	0
7	adiabatic	nocond	0.28
8	adiabatic	nocond	0
9	calculated	def	0.28
10	calculated	def	0
11	calculated	nocond	0.28
12	calculated	nocond	0

Table 3.3: DoE approach for thermal correlation

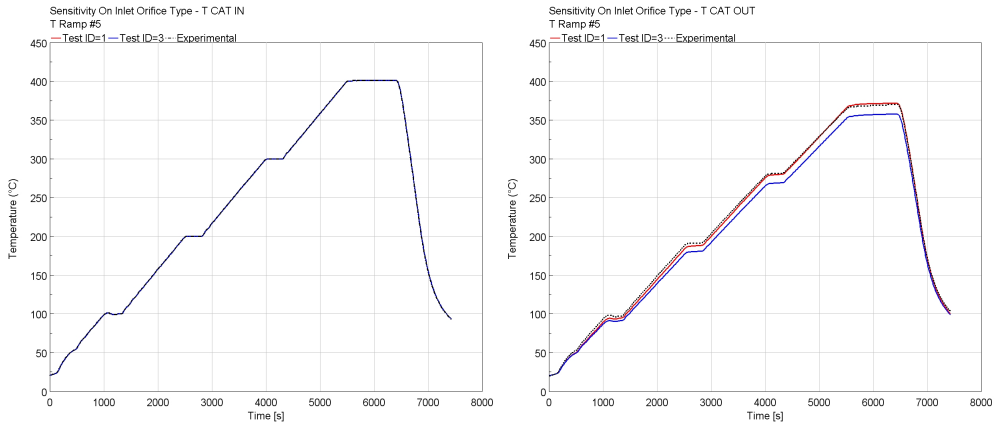
The Master Time Step of the solver (dt) has been fixed to **0.1 s** to be consistent with the frequency of acquisition of experimental data (10 Hz) and to avoid numerical errors in the heat transfer solution. In fact, the temperature gradient across the outer catalyst layers is solved with an explicit method that is decoupled from the 1D substrate solution made by the Advanced Adaptive (AA) chemistry solver. The AA chemistry solver benefits from large time steps, up to 10s, but the explicit thermal solver requires time steps less than 1 second (often as low as 0.01 seconds) [13].

The discretization length, that defines the number of sub-volumes into which the TWC part is divided and for which the Navier-Stokes equations are solved, has been fixed to **10 mm** after that a sensitivity analysis showed it had no relevant effects on the results. This value is actually quite large but anyway reasonable to be used at that point since no reactions were included yet.

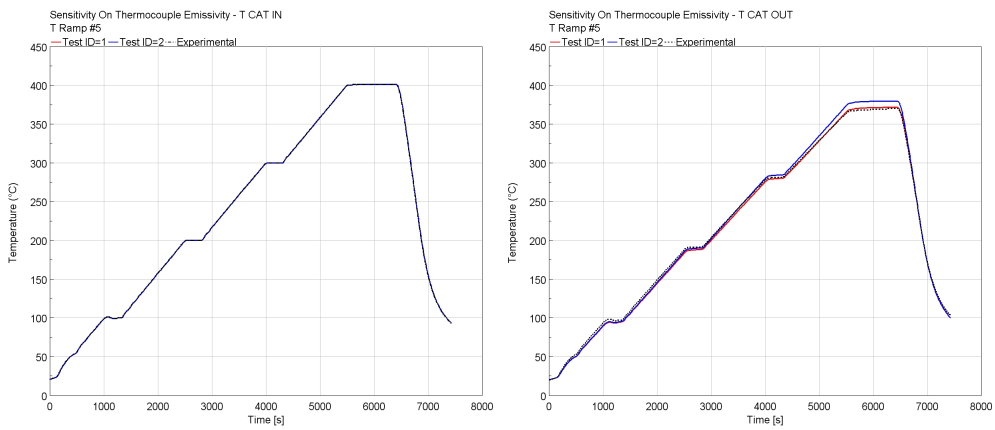
3.2 – Thermal Correlation



(a) Sensitivity on Inlet Pipe Wall Temperature Method



(b) Sensitivity on Inlet Orifice Type



(c) Sensitivity on Thermocouple Emissivity

Figure 3.3: DoE approach test results on T ramp #5

A Design of Experiments (DoE) approach, reported in table 3.3, was developed to investigate the effects of the remaining properties, i.e. inlet pipe wall temperature method, upstream TWC orifice type and thermocouple emissivity. In the setup of the "imposed wall layer property", the same T CAT IN profile given as inlet temperature trace was used.

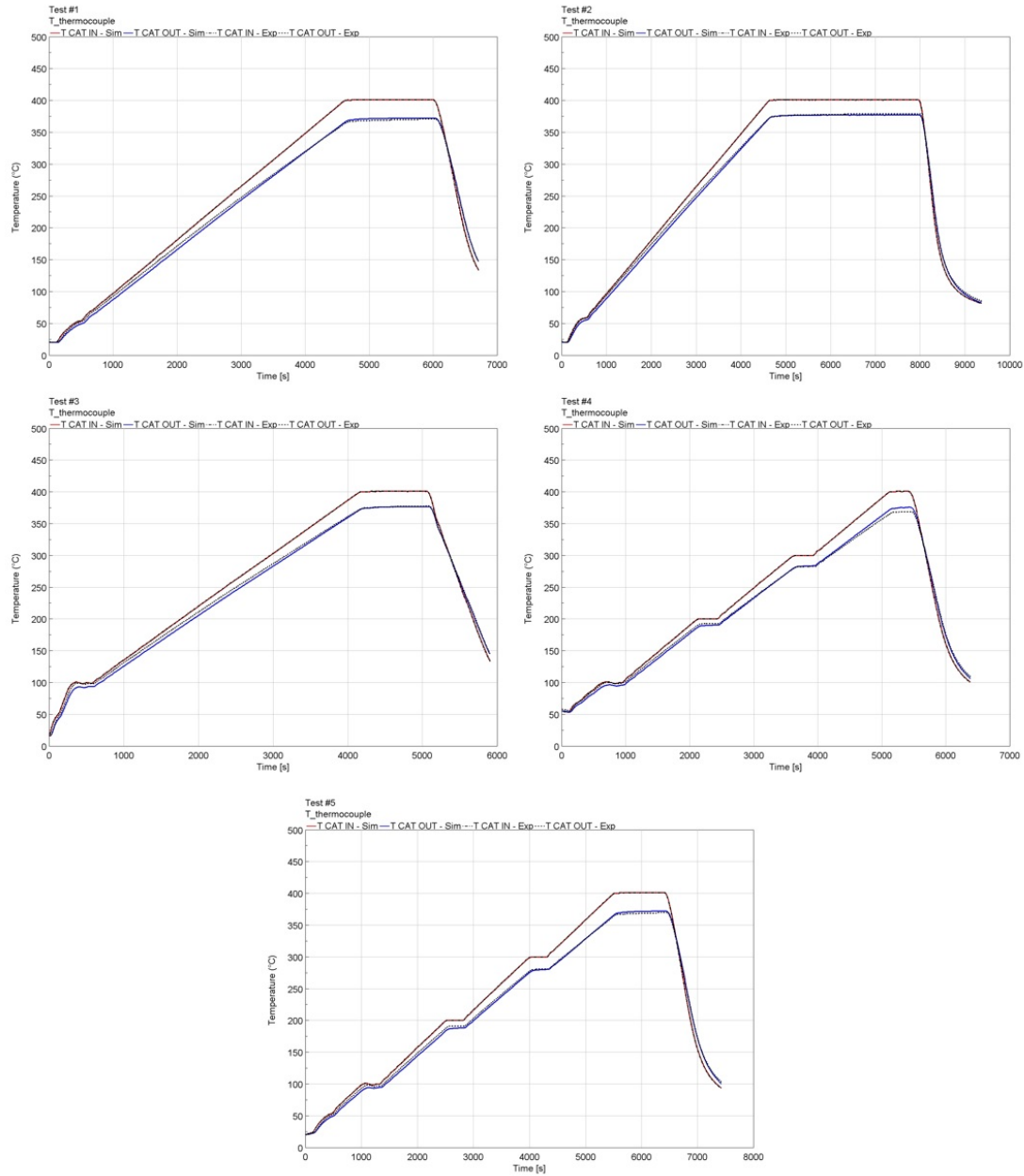


Figure 3.4: Thermal correlation results on the five warm-up tests

The results of the DoE analysis for the T ramp #5 are shown in figure 3.3. The best combination turned out to be one highlighted in bold in table 3.3. The outcome of the thermal correlation for the five T ramps can be seen in figure 3.4, with a closer look at T ramp #5 in figure 3.5. A quite good correlation between SGB experiments and GT-Suite simulations for all tests can be appreciated. The model is able to reproduce well the thermal losses occurring in the reactor system.

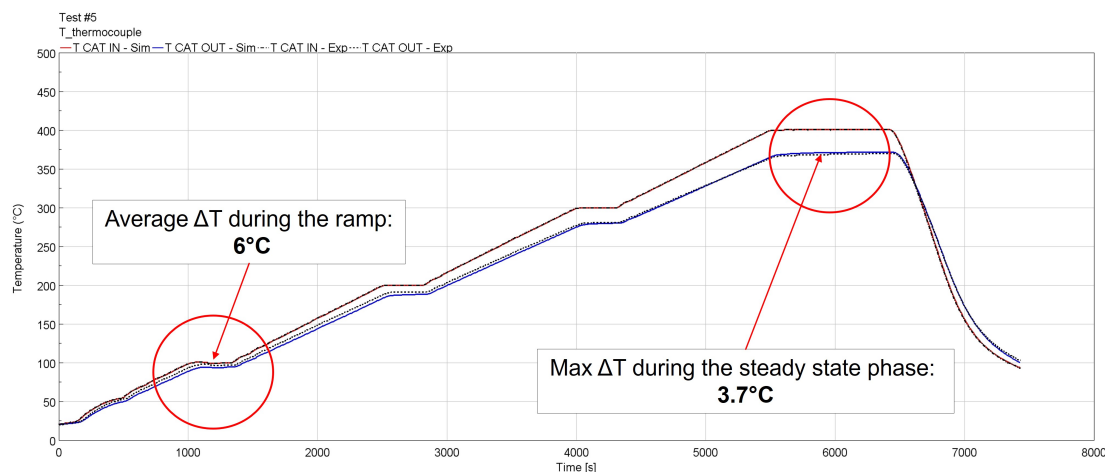


Figure 3.5: Thermal correlation results on T Ramp #5

3.3 Kinetics Scheme Calibration

The parameters targeted by the optimization were 31, including 3 dispersion factors, 11 pre-exponentials, 11 activation energies and 6 inhibition function exponents. The calibration sequence, reported in table 3.4, was defined according to the available data coming from the SGB experimental campaign reviewed in chapter 2. The aim was to minimize the number of parameters involved in each calibration step, thus simplifying as much as possible the optimization problem [7].

Step #1 involved the tuning of the reactions associated to O_2 storage and depletion on Ceria sites. In steps #2, #3, #4 and #5 the corresponding oxidation reactions were optimized. Step #6 was exploited to characterize reaction #9 together with the inhibition effects of the oxidizing species on Pt sites. Finally, reactions #5 and #6 were optimized in step #7.

To minimize the deviation from the experimental setup, the nominal inlet concentrations defined for each test protocol were corrected according to the actual measurements taken at reactor inlet, whenever it was necessary.

# Step	Reaction
1	OSC
2	OX: $CO + O_2$
3	OX: $C_3H_6 + O_2$
4	OX: $C_3H_8 + O_2$
5	OX: $CO + O_2 + H_2O$
6	OX: $CO + C_3H_6 + C_3H_8 + H_2O + O_2$
7	RED: $CO + NO$
8	RED: $C_3H_6 + NO$

Table 3.4: Kinetics scheme calibration sequence

3.3.1 Baseline Model Results

Before the beginning of the calibration process, a further sensitivity analysis on the TWC discretization length (dx) was performed, this time including the effects of the chemistry of the reactions. The goal was to find the best compromise between accuracy and computational time.

The full mixture performance test was simulated with the TWC model embedding the baseline R&S kinetics scheme [12].

The optimal value found for " dx " was **2mm**, corresponding to 45 catalyst sub-volumes. Below this value, no significant improvements were observed anymore. As expected, the previous value of 10mm, found in section 3.2, turned out to be too large to correctly reproduce the chemical phenomena.

Figure 3.6 and 3.7 shows the performances of **baseline scheme 1** (by R&S, 15 reactions) and **baseline scheme 2** (by Ferrari, 20 reactions).

Both the schemes were capable to correctly predict the overall conversion trends, except for the stall in the NO curve. However, the light-off temperatures were hugely overestimated. Apart from the C_3H_8 conversion profile, **baseline scheme 2** shows worse performances. The reason for this is that even if this scheme belongs to a catalyst with the same formulation, it was calibrated for other applications exploiting exhaust gas emissions from driving cycles. This scheme was thus used as a benchmark to appreciate the advantages introduced by the methodology adopted in this calibration activity.

3.3.2 Step #1: OSC Calibration

In this first step, the Cerium dispersion factor as well as the kinetics parameters of the reactions governing the storage of oxygen on Ceria sites during lean phases, reactions #10 & #19 (table 3.1), and the reduction of stored oxygen by means

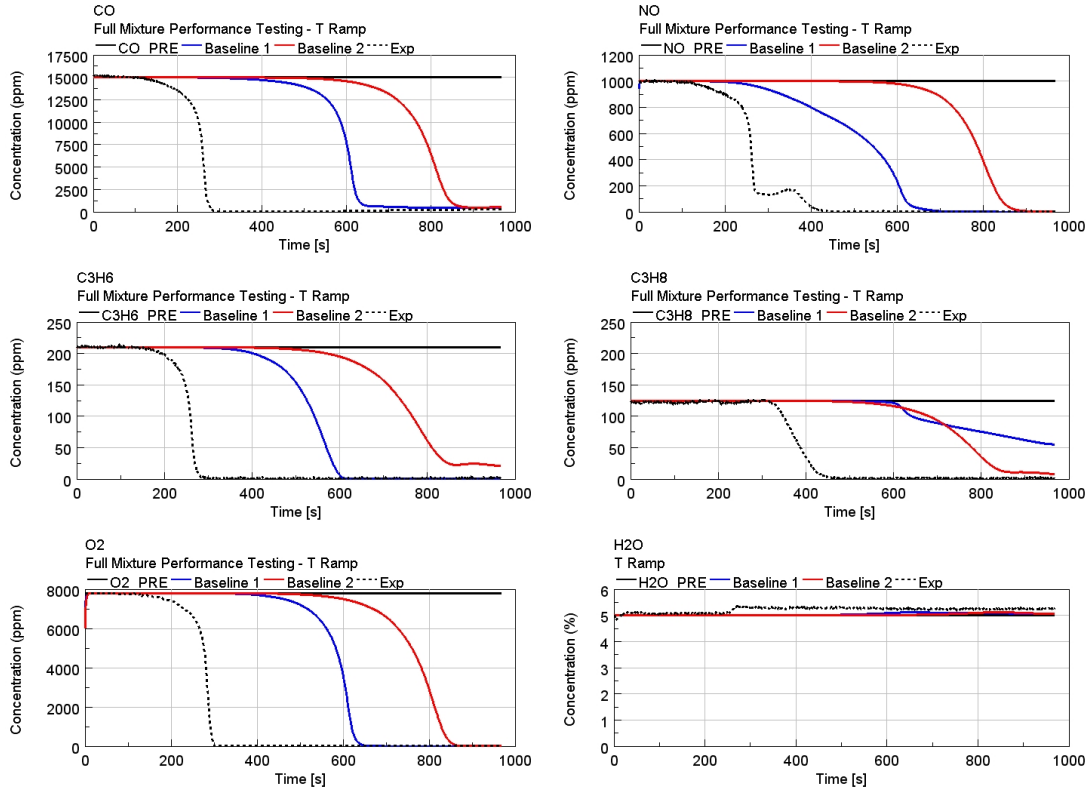


Figure 3.6: Full mixture performance testing. Baseline schemes (R&S and Ferrari). Experimental and simulated outlet species concentrations

of CO during rich phases, reactions #13 & #19 (table 3.1), were targeted by the optimization.

In principle, also C_3H_6 , C_3H_8 and H_2 are capable to consume the stored oxygen during rich phases, but unfortunately no experimental test including these species at the inlet was performed. Therefore, the remaining reactions on Ceria sites were left with their baseline parameters values.

The calibration was divided in two phases, according to what presented in [15]:

1. Tuning of the Cerium dispersion factor to match the lambda measurements during lean phases (figure 2.4) (oxygen refill in the TWC).
2. Optimization of the kinetics parameters of the reactions involving CO oxidation during rich phases to match the FTIR measurements of CO and CO_2 (oxygen purge in the TWC)

Since the lambda sensor embedded in the model did not work with just N_2 and O_2 and N_2 and CO as inlet species, a mathematical relation that provided lambda as

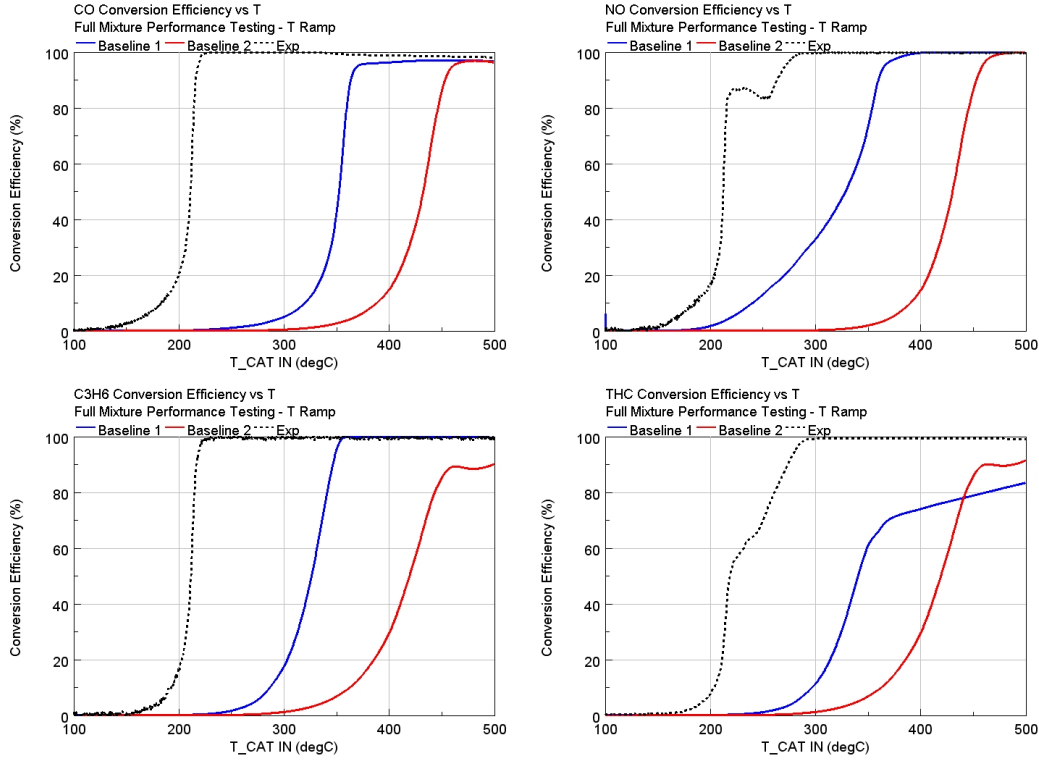


Figure 3.7: Full mixture performance testing. Baseline schemes (R&S and Ferrari). Experimental and simulated conversion efficiencies

a function of the CO and O_2 outlet concentrations was then found:

$$\lambda = 1 + \left(\frac{0.012}{0.25} \right) * [\%O_{2,OUT}] - 0.019 * [\%CO_{OUT}] \quad (3.7)$$

Experimental evidence showed that at $500^\circ C$ all the oxygen previously stored was consumed by the CO oxidation. By keeping constant the kinetics parameter of reactions #10, #13, #19 and tuning the ones of reaction #15, it was sufficient to manually calibrate the C_e dispersion factor so that the time interval to get $O_{2,OUT} = O_{2,IN}$ after the switch to lean mixture (O_2 break-off) coincided with the measurement reported in table 2.2. The value found with this method is **0.350**, that leads to a C_e loading of about $90 mol/m^3$.

Being these tests conducted under isothermal conditions, the reaction rates were constant during the experiments thus there was an infinite number of combinations of pre-exponentials and activation energies associated to each of them. It was then necessary to directly calibrate the reaction rates.

Subsequently, Arrhenius plots (figure 3.8) were employed to perform a linear regression of the optimized rates to extract the pre-exponentials and activation

energies (equation (3.8)) [8]. Actually, it turned out that only reaction #15 played a fundamental role, so the other reactions were not considered.

$$Rate = Ae^{\left(-\frac{E_a}{RT}\right)} \Rightarrow \ln(Rate) = \ln(A) - \left(\frac{E_a}{R}\right) \frac{1}{T} \quad (3.8)$$

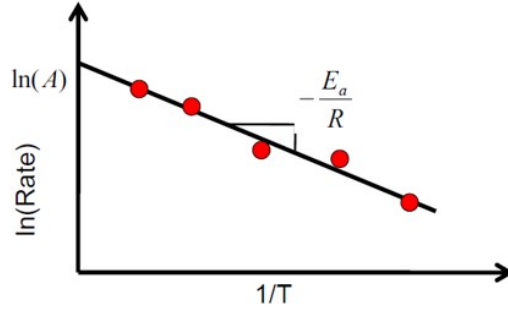


Figure 3.8: Example of Arrhenius plot [13]

The baseline values of the parameters of reaction #15, i.e. A_{15} & E_{a15} , together with the corresponding reaction rate constant at the three temperature levels are shown in table 3.5:

Baseline parameters values		Rate constant of reaction #15 k_{15}		
A_{15} [-]	0.1824	300°C	400°C	500°C
E_{a15} [kJ/mol]	31.768	2.322E-04	6.251E-04	1.303E-03

Table 3.5: Rate constant of reaction #15 (k_{15}) at the three OSC temperature setpoints

Table 3.6 reports the GA setup, while figure 3.9 shows the outcome of the linear regression.

	Parameter ID	Range for Optimization	
		Lower Limit	Upper Limit
Parameter	k_{15}	1.00E-04	1.00E+06
Number of Generations		20	
Population Size		10	
Tot. number of designs		200	

Table 3.6: OSC calibration - GA setup

The final optimized parameter values can be seen in table 3.7. Figures 3.10,

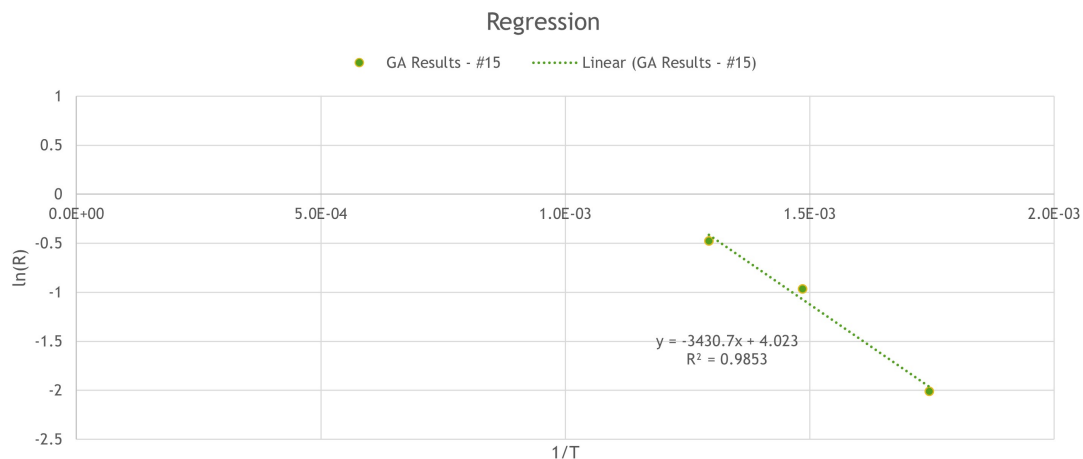


Figure 3.9: Arrhenius plot used for linear regression

3.11 and 3.12 show the optimized model results compared to the baseline scheme by R&S and Ferrari. Experimental O_2 concentrations are missing since the EXSA Analyser response for O_2 was too slow to be useful in OSC measurement.

Parameter	Unit	Optimized Value
Ce dispersion factor	[-]	0.350
A15	[-]	3.535E+04
Ea15	[kJ/mol]	64.812

Table 3.7: Step #1: OSC optimization results

With the baseline R&S kinetics scheme, there is almost no CO oxidation during the rich phase, even at the highest temperature. Although the optimized scheme shows a substantial improvement, there is still a quite huge underestimation in the CO oxidation, especially for tests #2 and #3. In fact, the GA was not able to find an optimal value for the rates of reaction #15 to provide an acceptable correlation for all the 3 tests. Apparently, it seems that there is no way to fit in a good manner the experimental data with the actual reaction kinetics. A possible reason for this is that the CO oxidation reaction rate get saturated above 400°C, a behavior that the kinetics scheme is not able to reproduce.

It is then necessary to modify the mechanism considering as a possible solution the implementation of two different Cerium sites: fastCe and slowCe, as done in other commercial software.

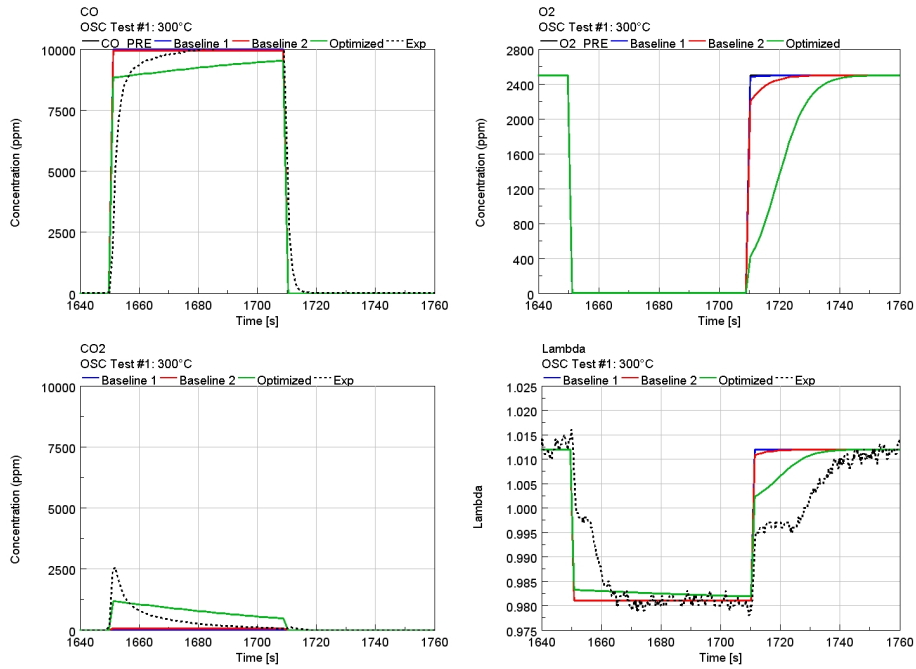


Figure 3.10: OSC test #1: 300°C. CO , O_2 , CO_2 and λ traces

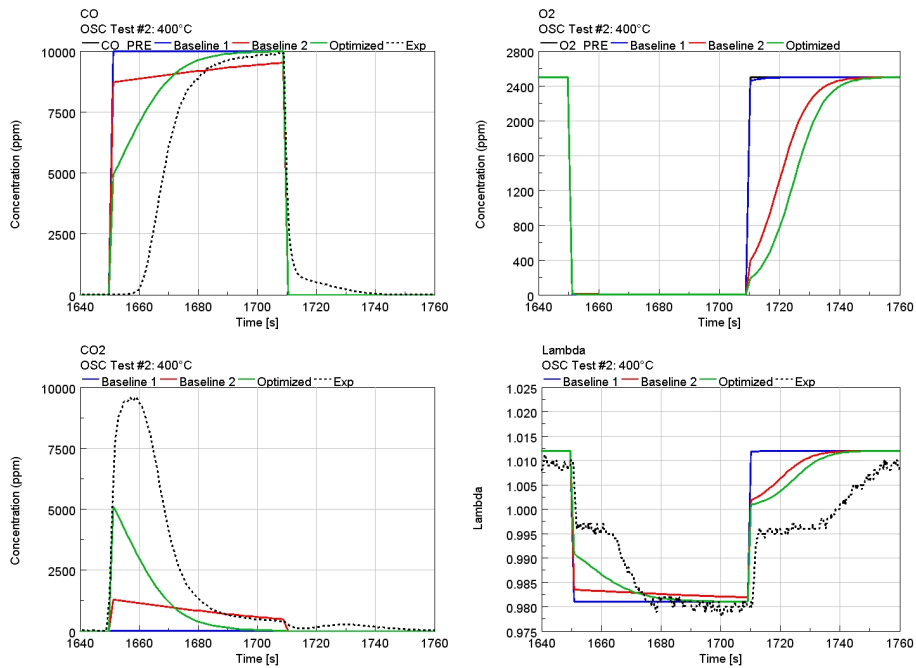


Figure 3.11: OSC test #2: 400°C. CO , O_2 , CO_2 and λ traces

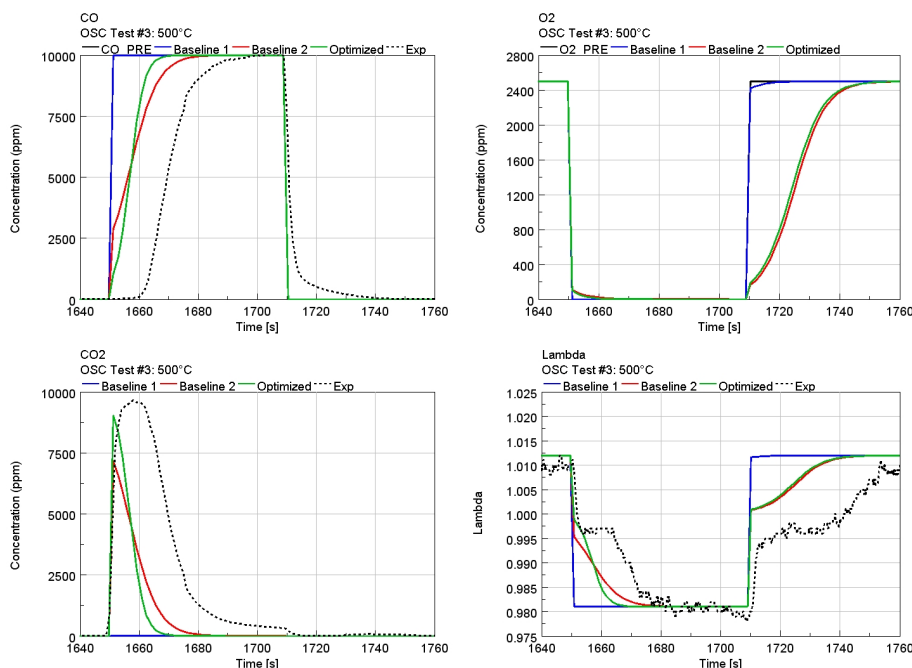


Figure 3.12: OSC test #3: 500°C. CO , O_2 , CO_2 and λ traces

Reactions associated to fastCe should be tuned to be active at lower temperatures (300°C). On the contrary, reactions associated to slowCe should be tuned to be active at higher temperatures (400°C and 500°C).

3.3.3 Oxidation Reactions Calibration

Step #2: $CO + O_2$

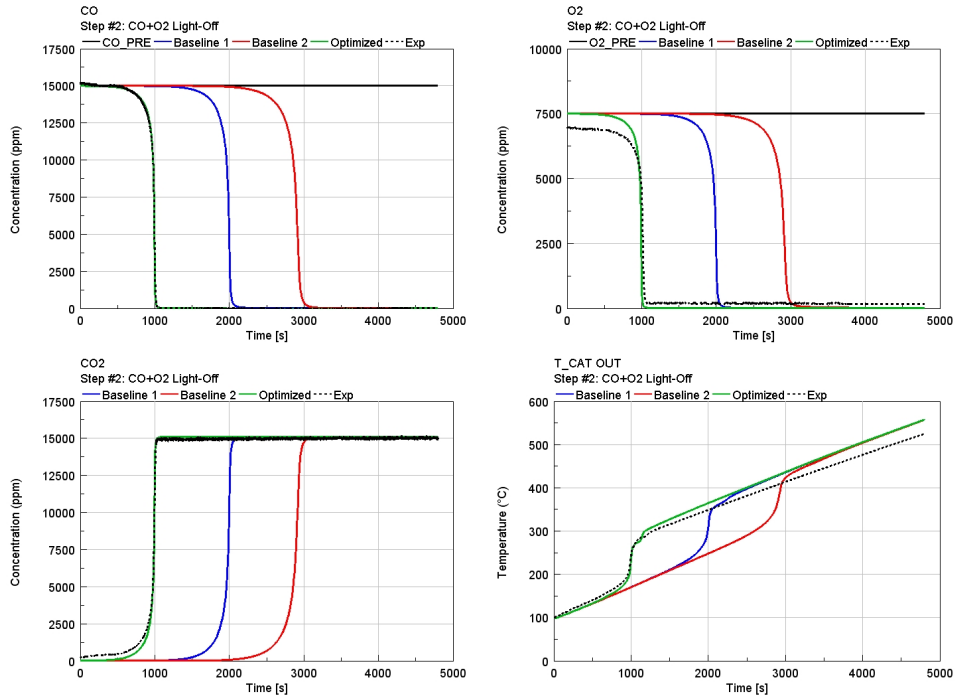
In this first step of oxidation reactions calibration, light-off test #1 (see table 2.6), which only included CO at the inlet, was used to tune reaction #1 parameters, A1 and Ea1, together with the Pd dispersion factor.

Parameter	Unit	Baseline Value	Range	Optimized Value
Pd disp. factor	[-]	0.1	0.1-0.35	0.247
A1	[-]	5.542E+13	$10^{12} - 10^{15}$	5.817E+13
Ea1	[kJ/mol]	121.450	100 - 150	106.553

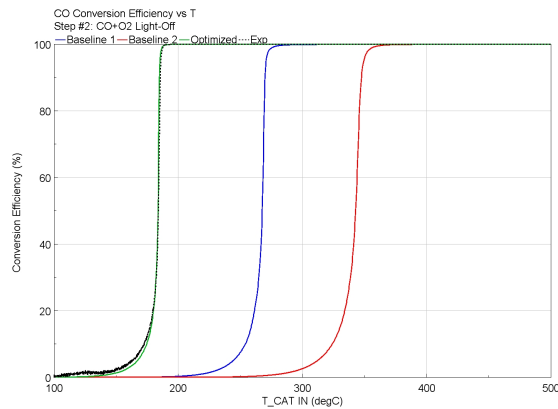
Table 3.8: Step #2: optimization results

The GA was set to target the CO experimental outlet concentration during the T ramp phase exploiting the "transient targeting" method. An initial run employing

20 generations and a population size of 10 individuals was exploited to identify the region of convergence of each parameter. A second run was then performed updating and tightening the range in order to increase the resolution of the algorithm. The total number of designs was thus 400. This two-step optimization approach was applied for all the subsequent calibrations.



(a)



(b)

Figure 3.13: $CO + O_2$ light-off test. (a) CO , O_2 , CO_2 and $T_{CAT OUT}$ traces. (b) CO conversion efficiency.

The baseline parameters, the optimization range and the optimized values can be seen in table 3.8.

Figure 3.13 (a) shows a comparison between measured and simulated outlet concentrations and temperature profiles. Figure 3.13 (b) shows a comparison between measured and simulated CO conversion efficiency. It is interesting to notice that although the high correlation level, the outlet catalyst temperature deviates from the experimental profile after full CO conversion is reached. This will require further investigation on the heat released by the reaction, that appears to be overestimated.

Step #3: $C_3H_6 + O_2$

Reaction #2 parameters, A2 and Ea2, were calibrated exploiting light-off test #2 (see table 2.6), which only included C_3H_6 at the inlet.

The GA was set to target the C_3H_6 experimental outlet concentration exploiting the "transient targeting" method. The output of the two-step optimization approach, involving 20 generations per each run, is reported in table 3.9.

Parameter	Unit	Baseline Value	Range	Optimized Value
A2	[-]	1.917E+15	$10^{14.5} - 10^{16.5}$	1.449E+16
Ea2	[kJ/mol]	129.530	110 - 130	121.227

Table 3.9: Step #3: optimization results

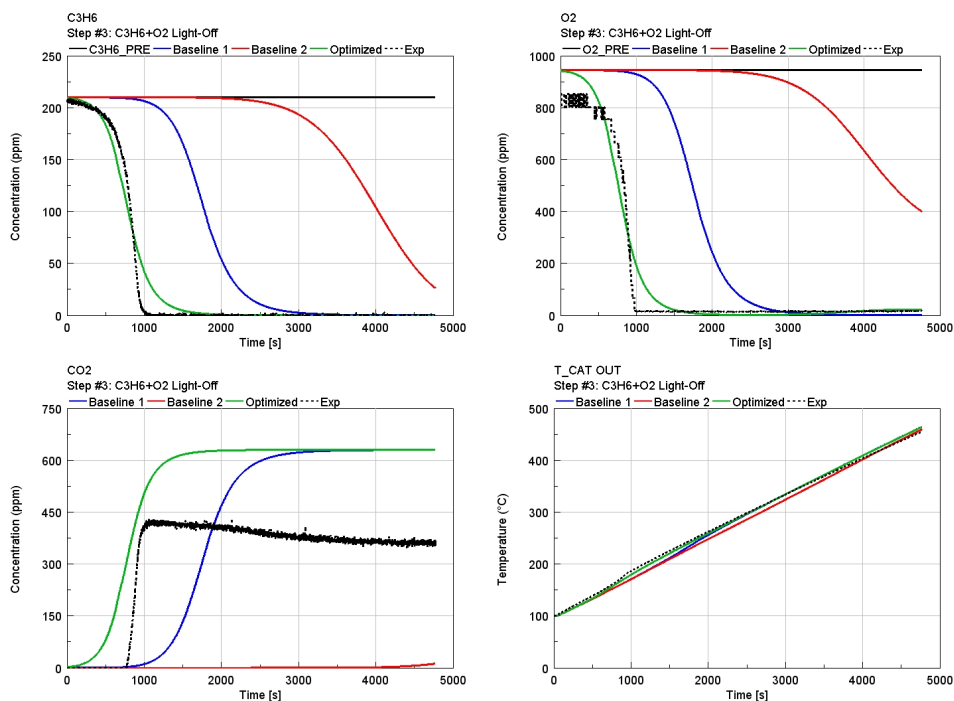
Figure 3.14 (a) shows a comparison between measured and simulated outlet concentrations and temperature profiles. Figure 3.14 (b) shows a comparison between measured and simulated C_3H_6 conversion efficiency. A substantial improvement with respect to the baseline scheme can be observed. However, the optimized curve of C_3H_6 conversion (in green) deviates from the experimental one (in black, dashed) when the 80% of efficiency is exceeded.

Step #4: $C_3H_8 + O_2$

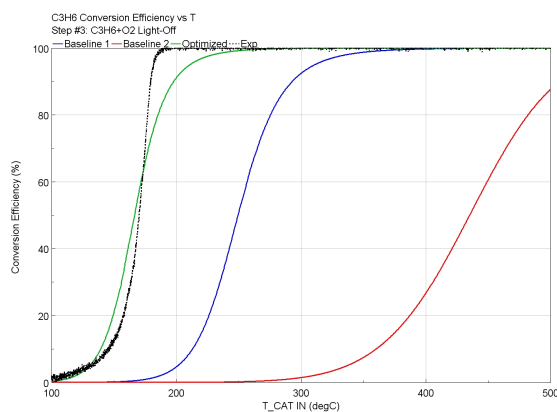
Parameter	Unit	Baseline Value	Range	Optimized Value
A3	[-]	6.404E+15	$10^{14.5} - 10^{17}$	1.178E+16
Ea3	[kJ/mol]	165.160	135.00 - 170	143.828

Table 3.10: Step #4: optimization results

In this step, light-off test #3 (see table 2.6) which only included C_3H_8 at the inlet, was used to calibrate reaction #3 parameters, A3 and Ea3.



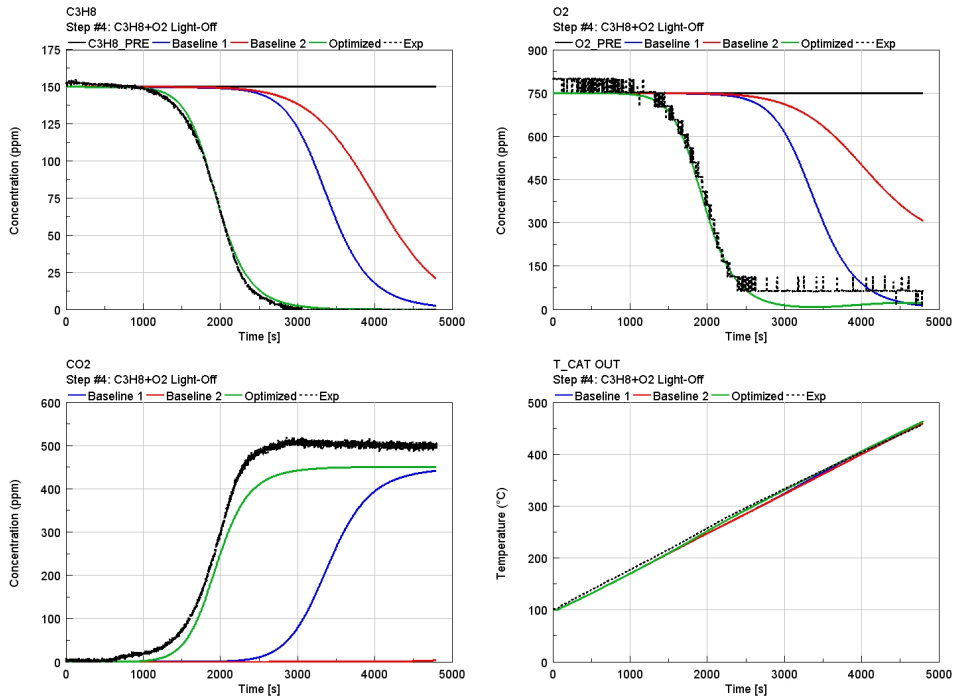
(a)



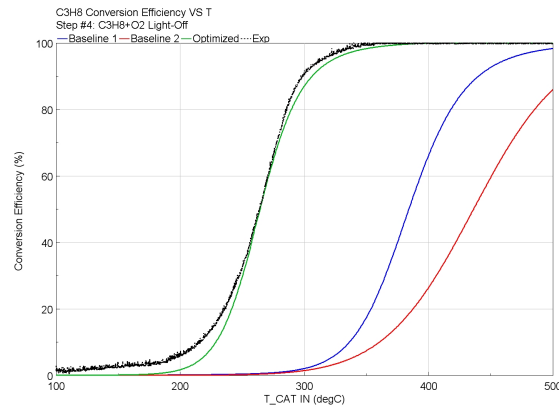
(b)

Figure 3.14: C₃H₆ + O₂ light-off test. (a) C₃H₆, O₂, CO₂ and T_{CAT OUT} traces. (b) C₃H₆ conversion efficiency.

The GA was set to target the C₃H₈ experimental outlet concentration exploiting the "transient targeting" method. The output of the two-step optimization approach, involving 20 generations per each run, is reported in table 3.10.



(a)



(b)

Figure 3.15: $C_3H_8 + O_2$ light-off test. (a) C_3H_8 , O_2 , CO_2 and $T_{CAT OUT}$ traces. (b) C_3H_8 conversion efficiency.

Figure 3.15 (a) shows a comparison between measured and simulated outlet concentrations and temperature profiles. Figure 3.15 (b) shows a comparison between measured and simulated C_3H_8 conversion efficiency. The correlation with the measured profiles is quite good. The T50 is matched, and the light-off trend shows little deviation from the experimental evidence.

Step #5: $CO + O_2 + H_2O$

Calibration of reaction #8 parameters, A8 and Ea8, was initially performed using experimental data from test #5 (see table 2.6), which only included CO and H_2O at the inlet.

The GA was set to target the experimental CO outlet concentration exploiting the "transient targeting" method. In order to be validated, the optimized parameters were then used to simulate test #6, which included CO , H_2O and O_2 at the inlet. Unfortunately, the outcome was not satisfying.

In fact, the experimental evidence showed that the additional presence of water in the feed (at 5%) results in a reduction in CO T50 of 17°C. This beneficial effect should not be due to the WGS reaction [14] since it is typically associated to much higher temperatures. Incorporating this behavior into the model could have been done by including water as a promotional term in a new kinetic expression for CO oxidation, or including a low temperature WGS reaction. A simpler solution was to perform a further optimization run on A8 and Ea8, which outcome is reported in table 3.11, this time directly on test #6.

Parameter	Unit	Baseline Value	Range	Optimized Value
A8	[-]	1.800E+05	$10^5 - 10^6$	1.718E+06
Ea8	[kJ/mol]	56.720	43 – 60	44.357

Table 3.11: Step #5: optimization results

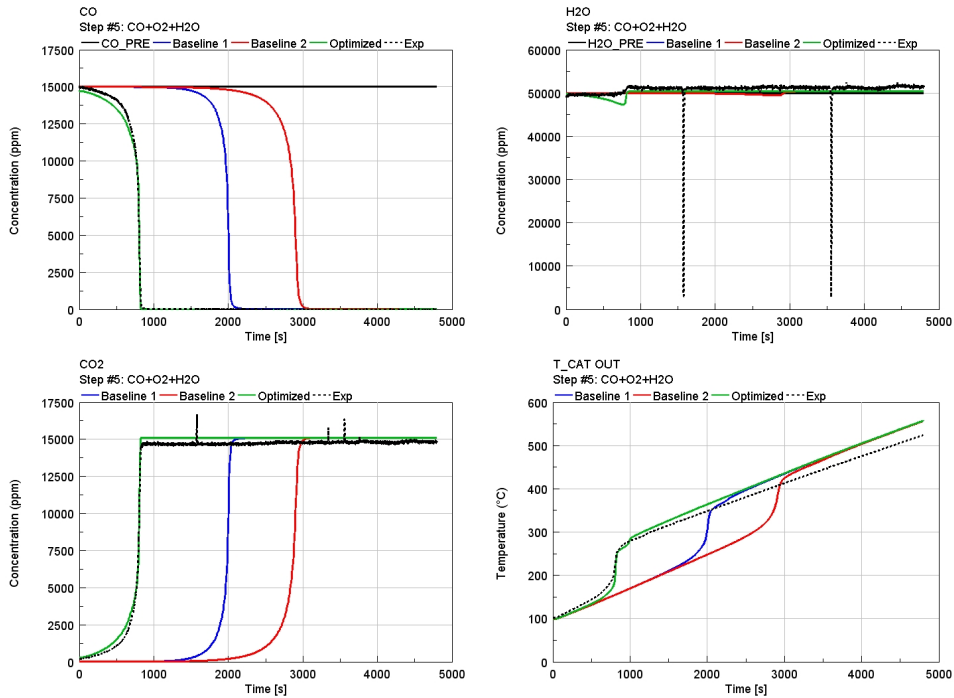
Figure 3.16 (a) shows a comparison between measured and simulated outlet concentrations and temperature profiles. Figure 3.16 (b) shows a comparison between measured and simulated CO conversion efficiency.

Step #6: $CO + C_3H_6 + C_3H_8 + H_2O + O_2$

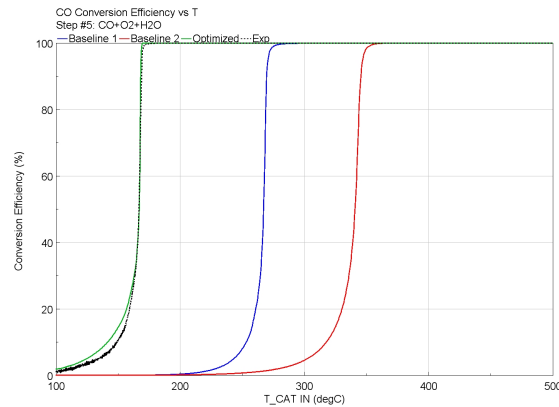
In this step, light-off test #7 (see table 2.6), in which were fed all the pollutant species except NO , was employed to characterize the inhibition effect between CO , C_3H_6 and C_3H_8 , all of which are competing to be oxidized on Pd sites. In particular, the parameters targeted by the optimization were the exponents of inhibition function $G1$, $G1a$, $G1b$ and $G1c$. Moreover, reaction #9 parameters, A9 and Ea9 were also calibrated.

The GA was set to minimize an objective function, defined according to (3.9):

$$F_{obj} = \int_0^{t_{end}} \left(\frac{CO_{sim,out} - CO_{exp,out}}{CO_{in}} \right)^2 + \left(\frac{C3H6_{sim,out} - CO_{exp,out}}{C3H6_{in}} \right)^2 + \left(\frac{C3H8_{sim,out} - C3H8_{exp,out}}{C3H8_{in}} \right)^2 dt \quad (3.9)$$



(a)

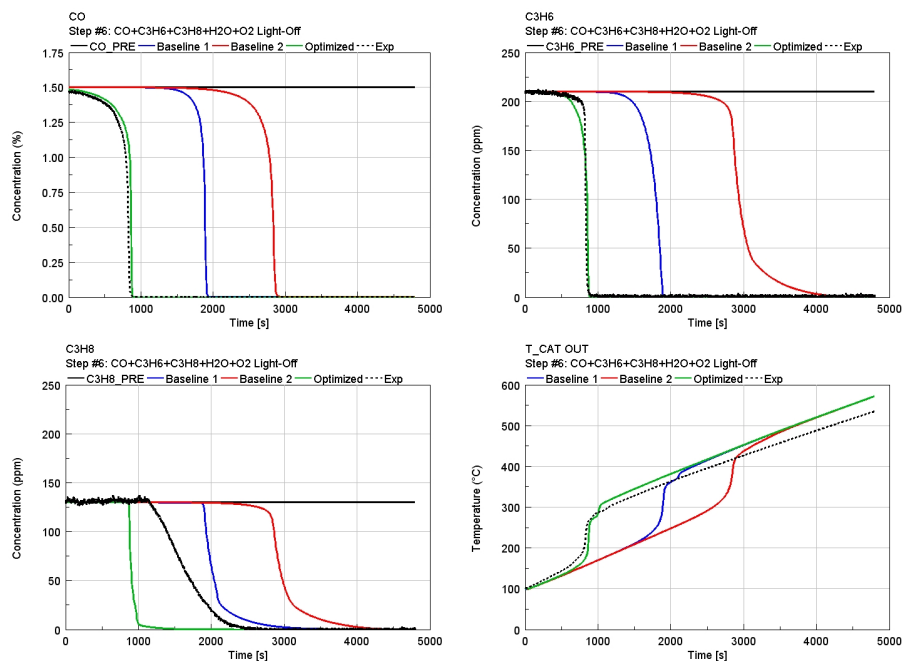


(b)

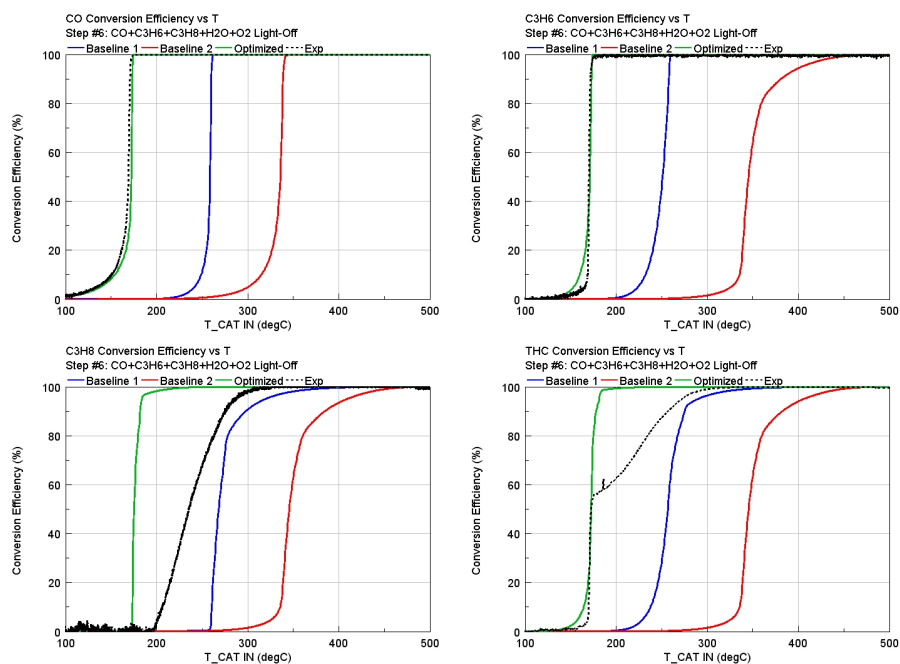
Figure 3.16: $CO + O_2 + H_2O$ light-off test. (a) CO , H_2O , CO_2 and $T_{CAT OUT}$ traces. (b) CO conversion efficiency.

The output of the two-step optimization approach, involving 20 generations and a population size of 20 individuals per each run, is reported in table 3.12. Figure 3.17 (a) shows a comparison between measured and simulated outlet concentrations and temperature profiles. Figure 3.17 (b) shows a comparison between measured and simulated CO , C_3H_6 , C_3H_8 and THC conversion efficiencies.

3.3 – Kinetics Scheme Calibration



(a)



(b)

Figure 3.17: $CO + C_3H_6 + C_3H_8 + H_2O + O_2$ light-off test. (a) CO , C_3H_6 , C_3H_8 and $T_{CAT OUT}$ traces. (b) CO , C_3H_6 , C_3H_8 and THC conversion efficiencies.

While CO and C_3H_6 conversions are quite well correlated, that is not the case for C_3H_8 , which conversion is hugely overestimated. A possible reason for this can be found in the definition of the inhibition function G1, in which a term that takes into account the C_3H_8 concentration is missing.

Parameter	Unit	Baseline Value	Range	Optimized Value
A9	[-]	1.230E+05	$10^4 - 10^6$	3.463E+05
Ea9	[kJ/mol]	81.920	60 – 100	97.154
G1a	[-]	485	200 – 1000	614
G1b	[-]	166	50 – 200	128.343
G1c	[-]	10163	5000 – 12000	6003.765

Table 3.12: Step #6: optimization results

3.3.4 Reduction Reactions Calibration

Step #7: $CO + NO$

Light-off test #8 (see table 2.6) was used to investigate the interaction between CO and NO . The Rh dispersion factor and the parameters of reaction #5, A5 and Ea5, as well as the NO inhibition effect on CO oxidation, inhibition function G3 exponents G3a and G3d, were object of the calibration.

Parameter	Unit	Baseline Value	Range	Optimized Value
Rh disp. factor	[-]	0.1	0.1-0.35	0.311
A5	[-]	2.857E+09	$10^8 - 10^{12}$	2.314E+11
Ea5	[kJ/mol]	52.374	35 – 65	59.649
G3a	[-]	485	350 – 700	629.464
G3d	[-]	3685	3000 – 4200	3128.629

Table 3.13: Step #7: optimization results

The GA was set to target the NO experimental outlet concentration exploiting the "transient targeting" method. The output of the two-step optimization approach, involving 20 generations per each run, is reported in table 3.13. Figure 3.18 (a) shows a comparison between measured and simulated outlet concentrations and temperature profiles. Figure 3.18 (b) shows a comparison between measured and simulated CO and NO conversion efficiencies. Even if the correlation was substantially improved with respect to the baseline scheme, there is an evident mismatch in the NO conversion in the high efficiency region.

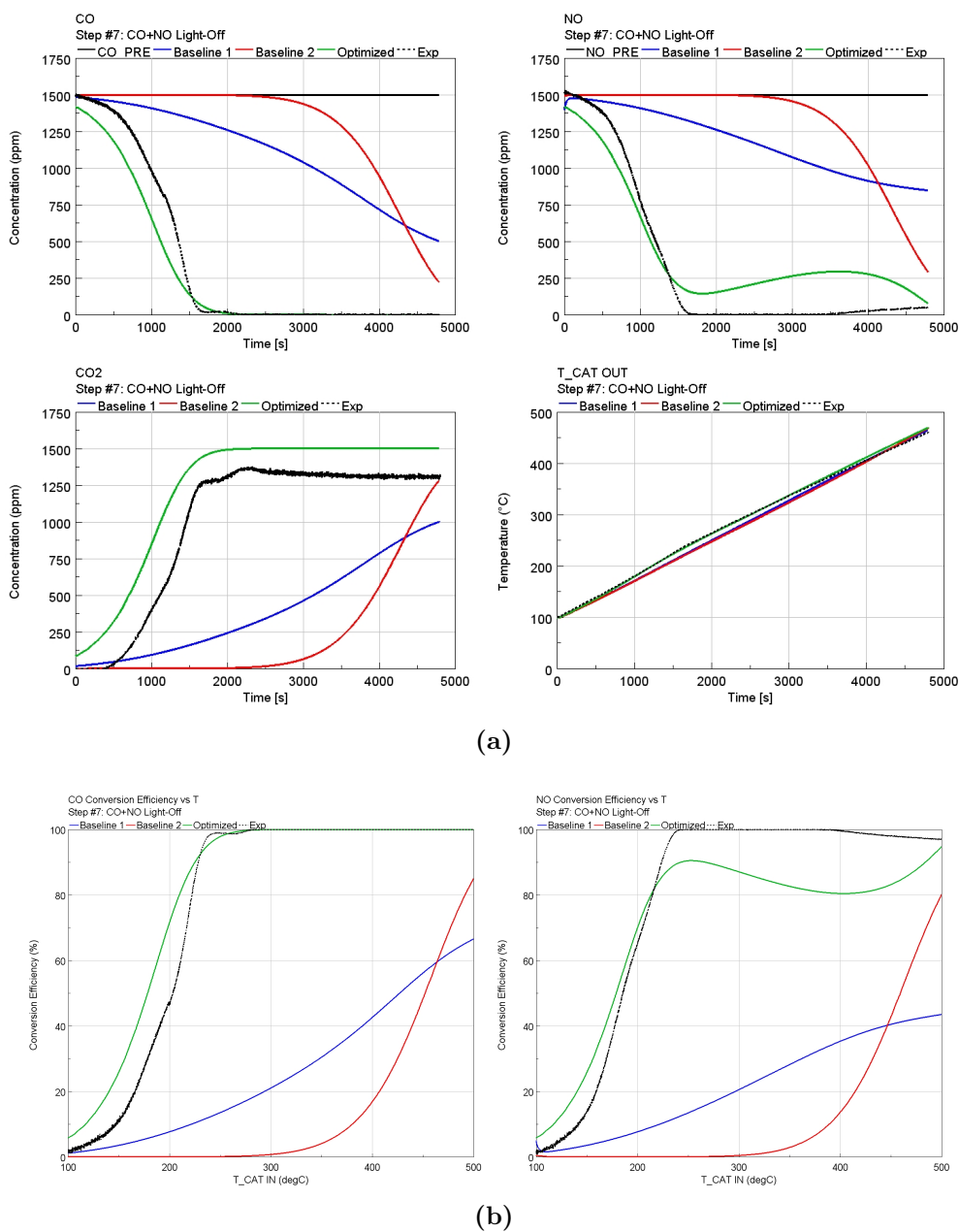


Figure 3.18: *CO* + *NO* light-off test. (a) *CO*, *NO*, *CO*₂ and *T_{CAT OUT}* traces. (b) *CO* and *NO* conversion efficiencies.

Figure 3.19 shows that *N*₂*O* in not negligible concentrations was measured at the catalyst outlet. Therefore, the fact that there is no reaction in the model that is able to predict *N*₂*O* formation is most likely cause of the observed deviation in the *NO* conversion.

A possible pathway can be defined according to [16]: $CO + 2NO \rightarrow CO_2 + N_2O$.

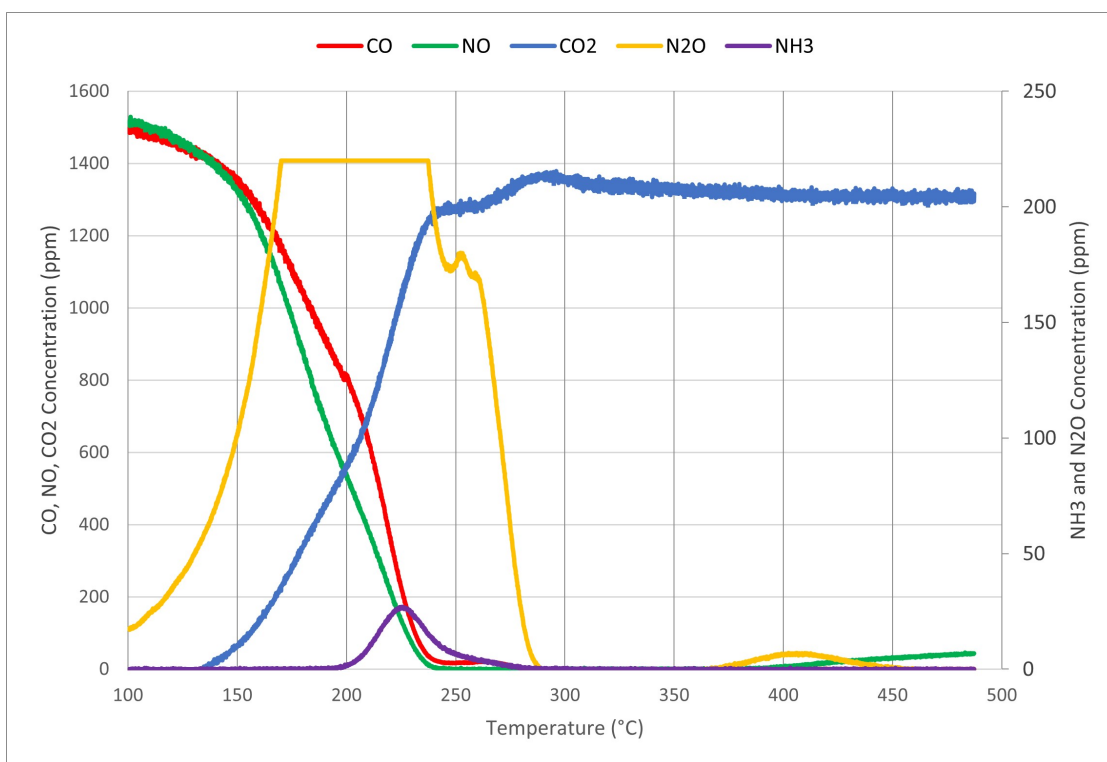


Figure 3.19: $CO + NO$ light-off test. Experimental outlet species concentrations

Step #8: $C_3H_6 + NO$

The last step involved the optimization of the parameters of reaction #6, A6 and Ea6, as well as the NO inhibition effect on C_3H_6 oxidation, taken into account by inhibition function $G3$ exponent $G3b$, exploiting light-off test #9 (see table 2.6). The GA was set to target the NO experimental outlet concentration exploiting the "transient targeting" method available in the software. The output of the two-step optimization approach, involving 20 generations per each run, is reported in table 3.14.

Parameter	Unit	Baseline Value	Range	Optimized Value
A6	[-]	2.994E+11	$10^{9.5} - 10^{13.5}$	3.776E+12
Ea6	[kJ/mol]	80.063	50 – 100	80.941
G3b	[-]	166	80 – 250	128.343

Table 3.14: Step #8: optimization results

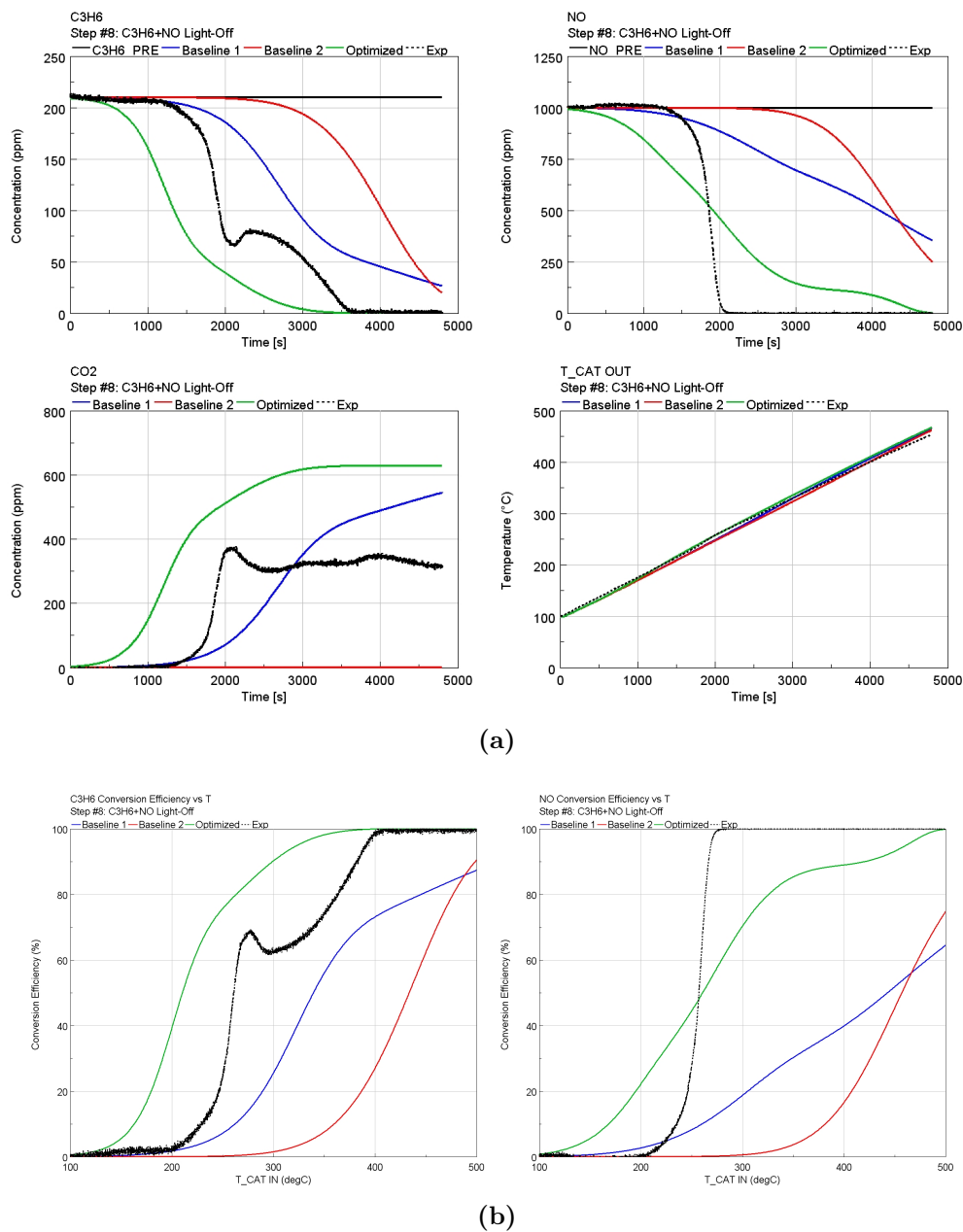


Figure 3.20: $C_3H_6 + NO$ light-off test. (a) C_3H_6 , NO , CO_2 and $T_{CAT OUT}$ traces. (b) C_3H_6 and NO conversion efficiencies.

Figure 3.20 (a) shows a comparison between measured and simulated outlet concentrations and temperature profiles. Figure 3.20 (b) shows a comparison between measured and simulated C_3H_6 and NO conversion efficiencies. It is evident that the actual kinetics scheme was not able to predict the phenomena

occurring in the TWC. Due to the lack of a proper pathway definition, the model was not capable of reproducing the stall of the C_3H_6 conversion efficiency, after which CO formation starts, neither the production of N_2O and NH_3 , experimentally observed.

In fact, figure 3.19 shows that there are actually two pathways for C_3H_6 oxidation. At the beginning of the T ramp, C_3H_6 is fully oxidized into CO_2 (in blue). By the time at which the C_3H_6 conversion efficiency approaches the 50%, it stalls and the C_3H_6 begins to be just partially oxidized into CO (in brown).

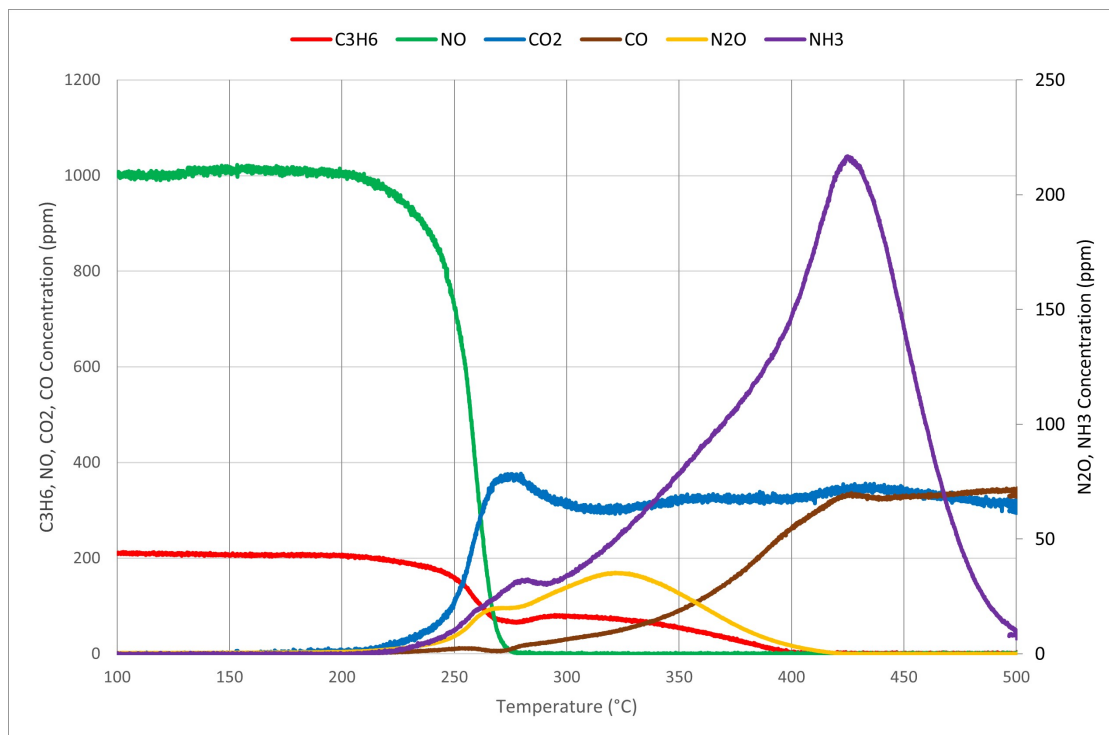


Figure 3.21: $C_3H_6 + NO$ light-off test. Experimental outlet species concentrations

3.4 Model Validation

The optimized kinetics scheme was validated on the same light-off full mixture performance test used to evaluate the performances of the baseline ones. This test includes the feeding of all the trace species reported in table 2.4.

As can be observed from figure 3.23, the optimized outlet gas temperature profile (green curve) is in good agreement with the experimental trace. The deviation in the last part of the ramp has to be accounted for the overestimation in the heat production of reaction #1 ($CO + O_2$), which is the strongest exothermic reaction

among those of oxidation.

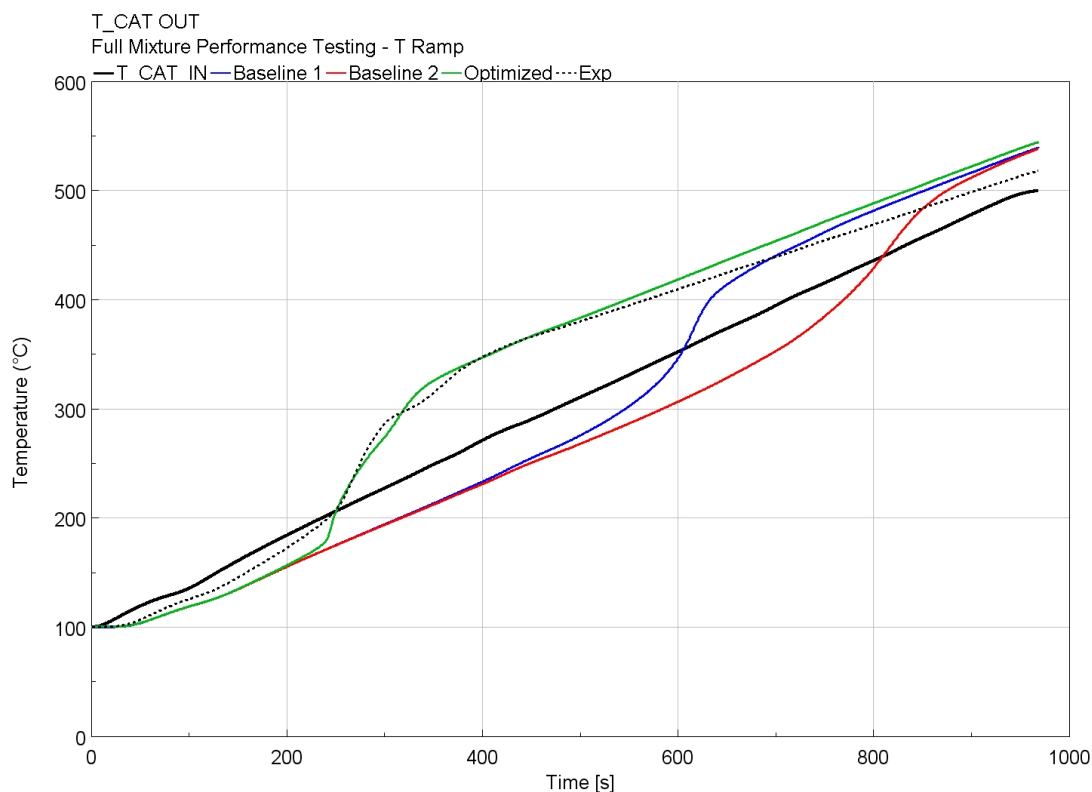


Figure 3.22: Full mixture performance testing. Optimized model. Experimental and simulated temperature profiles

The results of CO , C_3H_6 , C_3H_8 and NO concentration and conversion traces are shown in figure 3.23 and figure 3.24 respectively.

Concerning CO and C_3H_6 oxidation, model predictions are well correlated with the experimental measurements. While the CO slip occurring after 600s is correctly reproduced, in the case of C_3H_6 is slightly overestimated.

According to what reviewed in section 2.1.3, the experimental NO conversion is subjected to a stall in the high efficiency region around 85%. The subsequent achievement of 100% conversion is strictly associated with the oxidation of C_3H_8 . The fact that in the kinetics scheme there was neither a pathway capable to model the interaction among propane and nitrogen oxide nor between propane and water ($C_3H_8 + 3H_2O \rightarrow 3CO + 7H_2$ according to [16]), is most likely the cause of the observed deviation in the C_3H_8 and NO conversions.

As far as OSC is concerned, reactions on Ceria sites did not play a significant role being the inlet feed constant in composition and almost stoichiometric ($\lambda = 0.998$).

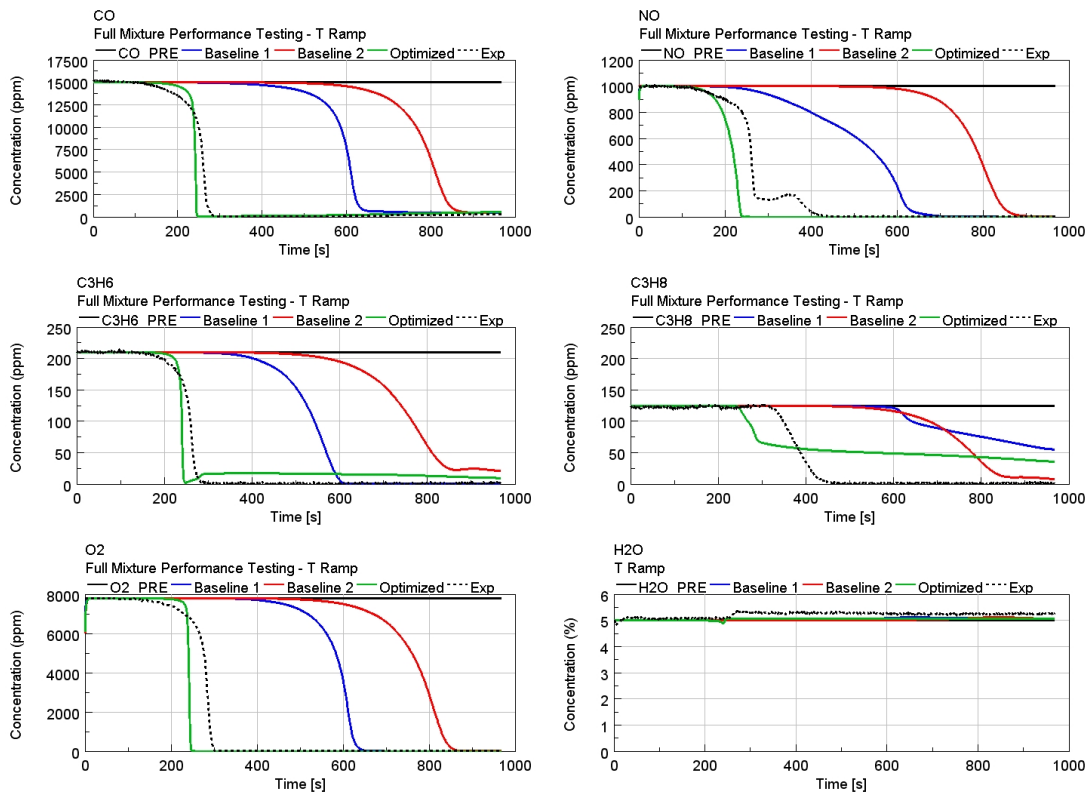


Figure 3.23: Full mixture performance testing. Optimized model. Experimental and simulated outlet species concentrations

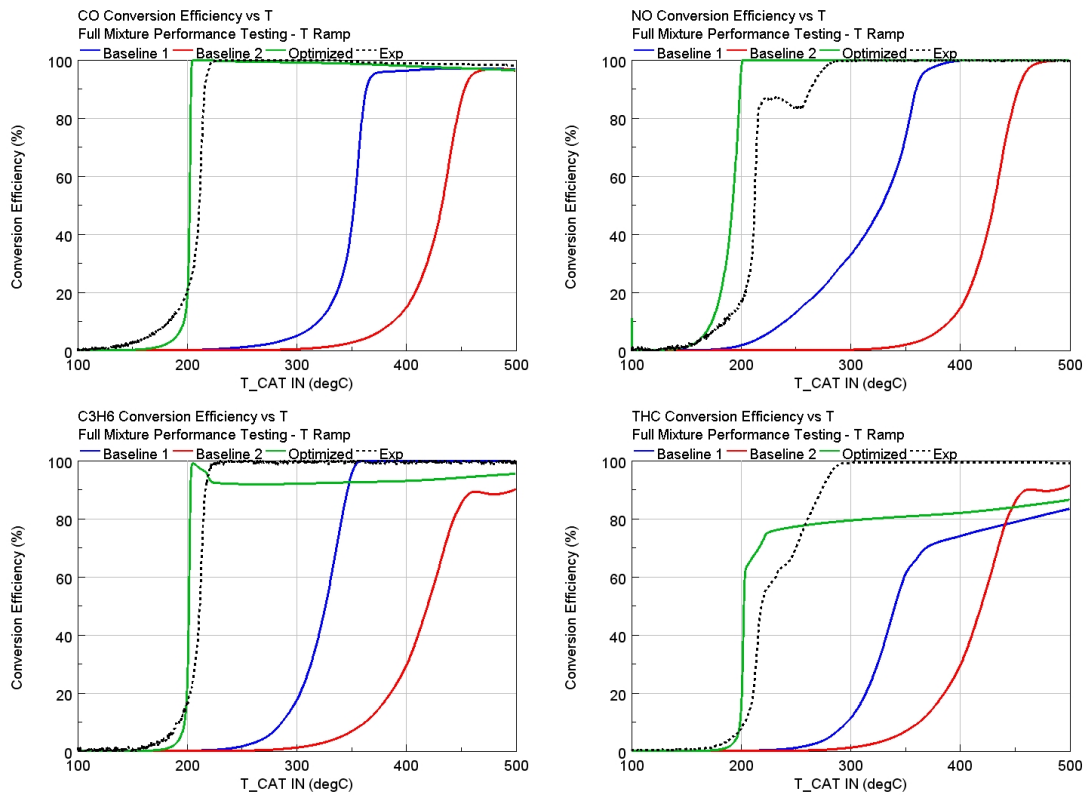


Figure 3.24: Full mixture performance testing. Optimized model. Experimental and simulated conversion efficiencies

Chapter 4

Conclusions

The purpose of this Master Thesis was to build and calibrate a 1D CFD reactor-scale model of a TWC currently adopted by Ferrari. The TWC was characterized by a dedicated extensive experimental campaign performed at the Synthetic Gas Bench (SGB) by the REACT laboratory of the Queen's University of Belfast (QUB).

The kinetics scheme has been defined starting from the one presented by Ramanathan & Sharma [12], which includes 15 reactions. To this scheme, five reverse reactions occurring on Ceria sites were added, for a total of 20 reactions.

The sequential calibration process began with a thermal correlation, necessary to correctly reproduce the heat losses occurring in the reactor. Then, the OSC behavior was optimized, followed by the tuning of the PGM reactions, including the oxidation and reduction ones. For this last phase were used light-off tests conducted under a temperature ramp from 100°C to 500°C and involving representative simple mixtures made of few selected species. This allowed to separately analyze and calibrate the main reactions occurring inside the catalyst.

The optimization tool employed was the Genetic Algorithm embedded in the simulation software, GT-SUITE. This tool turned out to be effective and fast in finding the optimal parameters for each calibration step, independently from the initial values.

The optimized kinetics scheme was validated over a light-off test involving a representative full mixture of the real exhaust gas at the inlet.

The results show a substantial improvement in the catalyst performance predictivity with respect to the baseline kinetics scheme. This confirms the benefits introduced by a calibration based on SGB experiments in contrast to the use of real exhaust gas emissions from driving cycles.

The model was able to correctly reproduce the thermal inertia and the heat losses occurring in the reactor system. The CO , C_3H_6 , C_3H_8 and NO concentration

trends underwent significant improvements, with the T50s, i.e. the temperatures at which each pollutant species reaches 50% of conversion efficiency, that are now much well correlated with the experimental evidence.

However, limitations directly related to the lack of secondary oxidation and reduction pathways in the definition of the kinetic scheme became evident from the calibration activity. Future steps will then focus on the implementation of the necessary reactions to predict C_3H_6 and C_3H_8 partial oxidation and to model $C_3H_8 - NO$ interaction as well as N_2O and NH_3 formation. Furthermore, the possibility to introduce two different Cerium sites, fastCe and slowCe, will be investigated to improve the OSC behavior.

Bibliography

- [1] Scott Lemon and Allan Miller. *Electric Vehicles in New Zealand: from Passenger to Driver?* May 2013 (cit. on p. 4).
- [2] George A. Lavoie, John B. Heywood, and James C. Keck. «Experimental and Theoretical Study of Nitric Oxide Formation in Internal Combustion Engines». In: *Combustion Science and Technology* 1.4 (1970), pp. 313–326. DOI: 10.1080/00102206908952211. eprint: <https://doi.org/10.1080/00102206908952211>. URL: <https://doi.org/10.1080/00102206908952211> (cit. on p. 5).
- [3] Delphine Bresch-Pietri. *Robust control of variable time-delay systems : Theoretical contributions and applications to engine control*. Dec. 2012 (cit. on p. 7).
- [4] *Schematic diagram of the three-way catalytic converter*. <https://www.open.edu/openlearn/science-maths-technology/science/chemistry/the-three-way-catalytic-converter/content-section-1.2.1>. Accessed: 2021-09-15 (cit. on p. 8).
- [5] *Emission Control Catalysts*. <https://dieselnet.com/tech/catalysts.php>. Accessed: 2021-09-15 (cit. on p. 9).
- [6] Angelo Onorati and Gianluca Montenegro. «1D Simulation Models for Aftertreatment Components». In: *1D and Multi-D Modeling Techniques for IC Engine Simulation*. 2020, pp. 387–416 (cit. on pp. 10, 11).
- [7] Federico Millo, Mahsa Rafigh, Francesco Sapio, Eduardo J. Barrientos, and Paolo Ferreri. «Application of Genetic Algorithm for the Calibration of the Kinetic Scheme of a Diesel Oxidation Catalyst Model». In: *International Powertrains, Fuels & Lubricants Meeting*. SAE International, Sept. 2018. DOI: <https://doi.org/10.4271/2018-01-1762>. URL: <https://doi.org/10.4271/2018-01-1762> (cit. on pp. 13, 37).

- [8] Federico Millo, Mahsa Rafigh, Francesco Sapio, Syed Wahiduzzaman, Ryan Dudgeon, Paolo Ferreri, and Eduardo Barrientos. «Modeling NO_x Storage and Reduction for a Diesel Automotive Catalyst Based on Synthetic Gas Bench Experiments». In: *Industrial & Engineering Chemistry Research* 57.37 (2018), pp. 12335–12351. DOI: 10.1021/acs.iecr.8b01813. eprint: <https://doi.org/10.1021/acs.iecr.8b01813>. URL: <https://doi.org/10.1021/acs.iecr.8b01813> (cit. on pp. 15, 41).
- [9] *ECE 15 + EUDC / NEDC*. https://dieselnet.com/standards/cycles/ece_eudc.php. Accessed: 2021-10-01 (cit. on p. 23).
- [10] *Worldwide Harmonized Light Vehicles Test Cycle (WLTC)*. <https://dieselnet.com/standards/cycles/wltp.php>. Accessed: 2021-10-01 (cit. on p. 23).
- [11] *EPA Federal Test Procedure (FTP-75)*. <https://dieselnet.com/standards/cycles/ftp75.php>. Accessed: 2021-10-01 (cit. on p. 23).
- [12] Karthik Ramanathan and Chander Shekhar Sharma. «Kinetic Parameters Estimation for Three Way Catalyst Modeling». In: *Industrial & Engineering Chemistry Research* 50.17 (2011), pp. 9960–9979. DOI: 10.1021/ie200726j. eprint: <https://doi.org/10.1021/ie200726j>. URL: <https://doi.org/10.1021/ie200726j> (cit. on pp. 30–32, 38, 61).
- [13] Gamma Technologies. *GT-SUITE Aftertreatment Manual* (cit. on pp. 32, 34, 41).
- [14] David S. Newsome. «The Water-Gas Shift Reaction». In: *Catalysis Reviews* 21.2 (1980), pp. 275–318. DOI: 10.1080/03602458008067535. eprint: <https://doi.org/10.1080/03602458008067535>. URL: <https://doi.org/10.1080/03602458008067535> (cit. on pp. 32, 49).
- [15] Augusto Della Torre, Gianluca Montenegro, Angelo Onorati, Stefano Paltrinieri, Federico Rulli, and Vincenzo Rossi. «Calibration of the Oxygen Storage Reactions for the Modeling of an Automotive Three-Way Catalyst». In: *Industrial & Engineering Chemistry Research* 60.18 (2021), pp. 6653–6661. DOI: 10.1021/acs.iecr.0c05744. eprint: <https://doi.org/10.1021/acs.iecr.0c05744>. URL: <https://doi.org/10.1021/acs.iecr.0c05744> (cit. on p. 39).
- [16] R. Holder, M. Bollig, D.R. Anderson, and J.K. Hochmuth. «A discussion on transport phenomena and three-way kinetics of monolithic converters». In: *Chemical Engineering Science* 61 (Dec. 2006), pp. 8010–8027. DOI: 10.1016/j.ces.2006.09.030 (cit. on pp. 54, 57).